

Recent Advances in Ultraviolet Nanophotonics: from Plasmonics and Metamaterials to Metasurfaces

Dong Zhao^{1,#}, Zhelin Lin^{2,#}, Wenqi Zhu^{3,4}, Henri J. Lezec³, Ting Xu⁵, Amit Agrawal^{3,4}, Cheng Zhang^{2,}, Kun Huang^{1,*}*

¹Department of Optics and Optical Engineering, University of Science and Technology of China, Hefei, Anhui 230026, China

²School of Optical and Electronic Information & Wuhan National Laboratory for Optoelectronics, Huazhong University of Science and Technology, Wuhan, Hubei 430074, China

³Physical Measurement Laboratory, National Institute of Standards and Technology, Gaithersburg, Maryland 20899, USA

⁴Maryland NanoCenter, University of Maryland, Maryland 20742, USA

⁵National Laboratory of Solid State Microstructures & College of Engineering and Applied Sciences and Collaborative Innovation Center of Advanced Microstructures, Nanjing University, Nanjing, Jiangsu 210093, China

[#]D. Z. and Z. L. contributed equally to this work.

^{*}To whom correspondence may be addressed. Email: cheng.zhang@hust.edu.cn or huangk17@ustc.edu.cn

Abstract

Nanophotonic devices, composed of metals, dielectrics or semiconductors, enable precise and high-spatial-resolution manipulation of electromagnetic waves by leveraging diverse light-matter interaction mechanisms at sub-wavelength length scales. Their compact size, light weight, versatile functionality and unprecedented performance are rapidly revolutionizing how optical devices and systems are constructed across the infrared, visible and ultraviolet spectra. Here, we review recent advances and future opportunities of nanophotonic elements operating in the ultraviolet region, which include plasmonic devices, optical metamaterials, and optical metasurfaces. We discuss their working principles, material platforms, fabrication and characterization techniques, followed by representative device applications in different areas such as imaging, sensing, spectroscopy, and wavefront shaping. We conclude this review by elaborating future opportunities and challenges of ultraviolet nanophotonic devices.

1. Introduction

“Ultraviolet” means “beyond violet”, where violet refers to the color of visible spectrum with the highest photon energy. Ultraviolet (UV) radiation was discovered by German physicist Johann Wilhelm Ritter in year 1801[1]. Ritter observed that invisible rays beyond the violet end of the visible spectrum had an even stronger interaction with silver chloride-soaked papers than the violet light, and therefore called these rays “de-oxidizing rays” to emphasize their chemical reactivity. Nowadays, UV radiation typically refers to the electromagnetic waves with free-space wavelengths between 10 nm and 380 nm, and can be further divided into five sub-bands (**Fig. 1a**), which are the near-UV range (UV-A; free-space wavelength range: $315 \text{ nm} \leq \lambda_0 \leq 380 \text{ nm}$; photon energy range: $3.26 \text{ eV} \leq E_0 \leq 3.94 \text{ eV}$), the mid-UV range (UV-B; $280 \text{ nm} \leq \lambda_0 \leq 315 \text{ nm}$; $3.94 \text{ eV} \leq E_0 \leq 4.43 \text{ eV}$), the deep-UV range (longer wavelength portion of UV-C; $190 \text{ nm} \leq \lambda_0 \leq 280 \text{ nm}$; $4.43 \text{ eV} \leq E_0 \leq 6.53 \text{ eV}$), the vacuum-UV (VUV) range (shorter wavelength portion of UV-C; $100 \text{ nm} \leq \lambda_0 \leq 190 \text{ nm}$; $6.53 \text{ eV} \leq E_0 \leq 12.40 \text{ eV}$), and the extreme-UV (EUV) range ($10 \text{ nm} \leq \lambda_0 \leq 100 \text{ nm}$; $12.40 \text{ eV} \leq E_0 \leq 123.98 \text{ eV}$). UV radiation can be produced by both natural objects such as sun, or artificial sources such as gas-discharge lamps, lasers (e.g., argon-ion laser, helium–cadmium laser, argon-fluoride excimer laser etc.), light emitting diodes [2-4], nonlinear crystals and materials [5-10], plasmas [11], and synchrotron [12].

UV light plays an irreplaceable role in both fundamental research and practical applications, ranging from spectroscopy, imaging, microscopy, quantum optics, and time keeping, to lithography, light therapy, micro-machining, and sterilization (**Fig. 1b**). For example, circular dichroism (CD) spectroscopy using near-UV light is widely used for characterizing the secondary structures of proteins [13], while CD spectroscopy using deep-UV light is largely employed during the exploration and quality evaluation of chiral pharmaceuticals [14, 15]. Similarly, UV absorbance spectrophotometry is widely used for nucleic acid quantization [16, 17]. Also, UV light sources have long been an essential component in different generations of lithography system, whose resolution depends critically on the wavelength of the employed UV source [18, 19]. Unlike electromagnetic radiations of lower frequencies, UV radiation can cause ionization and breakage of chemical bonds. Consequently, UV light is widely used for air purification, waste-water treatment, micro-organism and virus inactivation, etc. [20, 21]

So far, manipulation of UV light largely relies on conventional refractive or reflective optical elements. In contrast to diverse optical materials that are low-loss in the near-infrared (near-IR) and

visible spectra, suitable materials for the UV region (specially for the deep-UV and even shorter wavelength regions) are relatively limited, expensive and complicated to process. For instance, high-refractive-index materials are preferred for various optoelectronic applications including anti-reflection coatings, filters, waveguides, etc. Unfortunately, many high-refractive-index materials are characterized by a relatively narrow bandgap, resulting in a high absorption of UV light. Consequently, UV optical elements are limited in functionality, diversity, operational bandwidth, and manufacturability, in comparison to their near-IR and visible counterparts. While exploring new UV materials and associated manufacturing techniques to overcome the aforementioned limitations, researchers are also exploiting new strategies that are based on nanophotonic technology, including those based on plasmonics, metamaterial and metasurface concepts. Contrary to conventional optical elements which reflect, refract, or diffract a light beam with their spatially-varying shapes, nanophotonic devices modulate various parameters of an electromagnetic wave (*e.g.*, amplitude, phase or polarization state) by engineering their constituent subwavelength unit cells [22-25]. These nanoscale building blocks can be judiciously designed such that the entire device either exhibits a novel electromagnetic response rarely found in nature, or provides similar or even superior functionality compared to its conventional counterpart, but with a tremendously reduced size. Consequently, nanophotonic technology holds great potential in creating high-performance optoelectronic systems with novel functionality, low loss and compact footprint [26-28].

In this review, we summarize previous achievements of UV nanophotonics technology and discuss its challenges as well as opportunities. We will first elaborate on UV plasmonic devices by explaining their working principle, key characteristics, as well as associated excitation and detection techniques (Section 2). Then, we will review one representative meta-optics element, *i.e.*, metamaterial, and discuss its applications in realizing novel electromagnetic functionalities in the UV, including negative index of refraction and hyperbolic dispersion (Section 3). Afterwards, we show that a UV metasurface can be obtained when a volumetric three-dimensional (3D) UV metamaterial gets condensed to a two-dimensional (2D) layer, and discuss the relevant physical mechanisms, material choices, as well as fabrication methods (Section 4). Different applications of the aforementioned devices, ranging from plasmonics-based photodetection and Raman spectroscopy, to meta-optics-based light field manipulation (*e.g.*, flat lensing, beam bending, holographic projection), photoemission spectroscopy, and nonlinear signal generation, are surveyed

(Section 5). We conclude the review by discussing existing challenges and potential future directions of UV nanophotonics technology.

2. Ultraviolet Plasmonics

Excited by external electromagnetic radiation, certain electric conductors such as gold (Au), silver (Ag) or aluminum (Al) exhibit collective oscillations of the quasi-free electrons at the metal-dielectric interface [29] (**Fig. 2a**). These oscillations decay exponentially along the normal direction (*i.e.*, z) away from the interface into both the metal and the surrounding dielectric, but propagates like a quasi-particle bound to the interface (*i.e.*, x - y plane), thereby being named as surface plasmon polaritons (SPPs). The electric field of an SPP is tightly confined at the interface between the metal and dielectric (vacuum or air), which mathematically requires the pure imaginary z -component of wave vector \mathbf{k} ($|\mathbf{k}|=2\pi n/\lambda_0$, where n is the complex refractive index of the metal and λ_0 is the wavelength in vacuum). It means that, for a good metal supporting SPPs, its refractive index n has a dominating imaginary part and an extremely small real part, thus demanding a negative real part in the permittivity. Au and Ag show excellent SPP resonances in the near-infrared and visible wavelengths [30], while Al with its permittivity shown in **Fig. 2b** is more suitable for excitation of SPPs in the UV spectral range [31]. Other poor metals such as Ga, In, Sn, Tl, Pb and Bi have also been suggested as alternate UV plasmonic materials due to the negative real part of their permittivity in this spectral range [32]. Surprisingly, semiconductor Si has recently been found to support SPPs with a photon energy up to 11.4 eV [33, 34], which is located at the extreme ultraviolet wavelengths.

Due to the negative real part of the refractive index for plasmonic materials, SPPs have an imaginary in-plane (x or y) component of the wave-vector because of which they also decay exponentially as they propagate at the metal-dielectric interface. According to band structure of a metal, the interband transition of electrons is induced by incident photons, accompanying energy transfer to kinetic energy of the electrons [35]. During this process, the created hot carriers, electrons and holes, have a lifetime on the order of several tens of femtoseconds, which is too short to reuse for energy harvesting and detection before their disappearance. In addition, phonon resonance, electron-electron scattering and Landau damping also contribute to SPP absorption [35]. Although loss is inevitable for SPPs, the highly confined electric fields at the metal-dielectric interface offer significant field enhancement, which facilitates observation of weak physical effects such as Raman scattering [36], nonlinear process [37] and photocurrent creation [38].

A large volume of literature including books and review articles are available for the interested readers to learn more about SPPs [29, 30]. Excitation of SPPs in the visible, near-infrared and even longer wavelengths is typically achieved using prism coupling, grating coupling, highly focusing optical beam or near-field interaction [29], where auxiliary optics required for excitation is widely available. Although, in principle, ultraviolet SPPs can also be excited by using the above methods, strong material absorption of the UV light in conventional optics and low-efficiency of photodetectors has hindered development of ultraviolet optical systems. So, we constrain the discussion about the excitation of ultraviolet SPPs to two approaches: using transverse-magnetic (TM) polarized plane-wave illuminating metals from the dielectric substrate side (**Fig. 2c**), and using accelerated high-energy electron beams (**Fig. 2d**).

The photon approach utilizes TM polarized light to illuminate a thin Al film on a transparent substrate at an incident angle of θ , from the substrate side. SPPs can be excited when the momentum conservation relationship between the incident light and SPP is satisfied [29], *i.e.*, $k_{SPP} = k_0 n_d \sin \theta$, where k_0 is the wave number of the operating wavelength in vacuum, n_d is the refractive index of the transparent substrate, the wavenumber of the SPP $k_{SPP} = k_0 [\epsilon_r \epsilon_s / (\epsilon_r + \epsilon_s)]^{1/2}$, ϵ_r is the real part of the refractive index of Al and ϵ_s is the permittivity of material (usually air) above the Al film (**Fig. 2c**). In this configuration, SPPs are excited only at the top interface between air and metal film via tunneling effect, which requires that the thickness of the metal film is smaller than the skin-depth, usually several tens of nanometers. The nearly perfect coupling from a TM polarized light into the SPPs can be achieved by optimizing the thickness of metal film, the incident angle θ and the operating wavelength, resulting in a null reflection of incident light. To observe the coupled SPPs, one can use scanning near-field optical microscopy (SNOM), which, however, has not been reported at the ultraviolet wavelengths. Instead, Gryczynski *et al.* employed a reverse process where SPPs are first excited by the fluorescence emission from Deoxyribonucleic Acid (DNA) base analogue 2-aminopurine and then transferred into the free-space propagating waves at an out-coupling angle of 59° , resulting in observation of an optical cone with narrow width at a free-space wavelength of 370 nm [39].

High-energy electrons incident on metallic nanostructures can also excite plasmon resonances through oscillating free-carriers (**Fig. 2d**), meanwhile also creating a far-field radiation referred to as cathodoluminescence (CL) [40]. Since the CL intensity depends on the local density of states (LDOS), its measurement enables mapping of plasmon modes with a spatial resolution of

few nanometers, benefitting from focused electron beams. Due to its high spatial resolution, electron-beam excitation is the most efficient approach to study plasmonic behavior of individual or multiple nanostructures at ultraviolet wavelengths [41]. In addition, use of high-energy electrons has another advantage of simultaneous excitation and detection of ultraviolet plasmon. For example, CL images of the LDOS in an Al nanorod (**Fig. 2e**) can reveal transverse and longitudinal plasmonic modes through analysis of the scattering spectrum of CL radiation [41]. The excited transverse mode has a maximum scattering intensity at a photon energy of ≈ 2.6 eV (**Fig. 2f**). In contrast, the longitudinal mode is mapped at a UV wavelength with photon energy of ≈ 4.3 eV.

3. Ultraviolet Metamaterials

Metamaterials typically refer to artificial 3D, volumetric media composed of bulk metallic and/or dielectric constituent elements. Optical metamaterials exhibit electromagnetic responses that are not found in nature and are radically different from those of their constituent materials. For example, a metamaterial acting as a left-handed (LH) or negative-index optical medium can sustain backwards electromagnetic waves, leading to several counter-intuitive phenomena such as negative refraction, reverse Doppler and Vavilov–Cherenkov effects as well as negative radiation pressure [42-44]. A LH medium is characterized by a complex electric permittivity ϵ and a complex magnetic permeability μ that are simultaneously negative in their real parts. When an electromagnetic plane wave propagates inside a LH medium, the direction of power flow (defined by the time-averaged Poynting-vector \mathcal{S}) is opposite to that of phase-front propagation (defined by the wave-vector \mathbf{k}). This yields a “backwards wave” described by a mode index (phase refractive index $n = -\text{Re}[\sqrt{\epsilon \cdot \mu}]$) which is negative.

Media with a LH electromagnetic response, though not found to exist in a naturally occurring state yet, are compelling because they entertain the possibility of realizing potentially useful functions such as flat-lensing [42] and Veselago-Pendry superlensing [45]. This has triggered a quest to achieve LH electromagnetic responses via the use of artificial metamaterials, which are usually composed of arrays of lithographically-shaped metal-dielectric resonators with deep-subwavelength periodicity, and designed for operation at frequencies ranging from the microwave [44, 46] up to the red-end of the visible [47]. However, the corresponding negative refractive index is typically narrowband and strongly angle-dependent, ruling out straightforward use in most potential applications relying on broad-angle off-axis propagation, such as flat lensing and superlensing.

Moreover, achieving a resonator-based LH response at higher frequencies of interest for imaging and lithography applications, such as at UV frequencies, is difficult due to fabrication constraints related to miniaturization of resonator dimensions.

An alternative scheme for implementing metamaterials with LH responses is to exploit the bulk-plasmon and surface-plasmon resonances of constituent metal volumes and metal-dielectric interfaces. Using this approach, a metal-dielectric-metal (MDM) plasmonic waveguide was first employed to create a “two-dimensional” LH metamaterial with an isotropic negative index of refraction in the waveguide plane, at green and blue frequencies [48]. The ω - k dispersion diagram (**Fig. 3a**) of the plasmon mode in an MDM waveguide exhibits a branch of negative slope (corresponding to a negative refractive index) between the bulk plasmon frequency (ω_p) and the surface plasmon resonance frequency (ω_{sp}). The high-frequency cutoff for the LH response occurs at ω_p , determined solely by the constituent metal. Therefore, choosing a metal with high ω_p (e.g., Ag, Al) can push the LH response to the UV or deep-UV spectral range. In addition, the low-frequency cutoff occurs at ω_{sp} , which is determined by both the constituent metal and surrounding dielectric, and at the same time, is the frequency at which the real part of the relative permittivity of metal is equal in amplitude but opposite in sign to that of the surrounding dielectric. Therefore, choosing a high-index dielectric such as TiO₂ and Si₃N₄ can push the LH response to the center of the visible spectral range. Silicon (Si), which is another high-index dielectric, can also push the LH response to the red-end of the visible. However, the above-bandgap absorption in Si results in a LH metamaterial with comparably high loss. A clever 2D negative refraction experiment (operating at free-space wavelength $\lambda_0 = 514$ nm) in an MDM geometry using Au-Si₃N₄-Ag as the constituent materials was performed (**Fig. 3b**) [48]. The clear illustration of negative refraction in this experiment represented the first experimental evidence of negative-index supported by the plasmon-mode in an MDM waveguide.

It is worthwhile to note that the LH plasmon mode in an MDM waveguide has an antisymmetric mode-profile (**Fig. 3c**), and therefore, can only be excited at non-normal incidence angles. To circumvent this limitation and to further achieve a bulk, volumetrically quasi-isotropic negative index of refraction in all three-dimensions, an alternative approach based on periodically stacked pairs of plasmonic waveguides with an MDMDM configuration was proposed (**Fig. 4a**) [49] and experimentally implemented in the UV for TM-polarized light (**Fig. 4b**) [50]. The experimentally realized 3D metamaterial was designed to exhibit a quasi-isotropic refractive index

of -1 at a UV free-space wavelength of $\lambda_0 = 364$ nm, and was fabricated by sputtering alternating layers of Ag and TiO₂ onto a fused-silica substrate. The MDMDM geometry can simply be thought of as two coupled MDM stacks, such that the mode becomes symmetric (**Fig. 4c**) and can thus be excited at any angle of incidence both along the plane of the layers and orthogonal to them – making the metamaterial behave as a volumetric bulk media with an associated quasi-isotropic index (similar to other isotropic media such as glass or free-space). In addition to performing negative refraction experiments to determine the refractive index (**Fig. 4d**), researchers further utilized this planar multilayer platform to demonstrate a Veselago flat-lens operating in the UV for the first time (**Fig. 4e**). These experimental realizations of negative refraction and flat-lensing using planar multilayer stack of alternating thin films of metal and dielectric represents a paradigm shift in how large-area planar metamaterials can be conceived without relying on complex lithographic patterning requirements.

Remarkably, dispersion engineering with such a multilayer approach is not just limited to achieving quasi-isotropic negative index of refraction. Instead, simple tweaking of the layer thicknesses can result in the media acting as a hyperbolic metamaterial (HMM) [51-53]. An HMM is a uniaxial effective medium described by an isotropic relative magnetic permeability $\mu = 1$ and diagonal relative electric permittivity tensor that obeys $\varepsilon'_\perp \varepsilon'_\parallel < 0$, where $\varepsilon_\perp = \varepsilon'_\perp + i\varepsilon''_\perp$ and $\varepsilon_\parallel = \varepsilon'_\parallel + i\varepsilon''_\parallel$ are respective complex effective relative permittivities for electric field components perpendicular and parallel to the anisotropy axis of the HMM. Depending on which of the two permittivity components, ε'_\perp or ε'_\parallel , is negative results in a type I ($\varepsilon'_\parallel < 0$) or type II ($\varepsilon'_\perp < 0$) HMM, either of which can quite elegantly control and/or filter the wavevectors of light propagating inside the HMM. This has led to the use of HMMs in a variety of applications from creating ultra-small cavities [54], promoting spontaneous emission [55, 56] or stimulated emission [57], engineering thermal emission [58, 59], achieving enhanced absorption [60], realizing sub-diffraction imaging [61, 62] and facilitating asymmetric transmission [63].

4. Ultraviolet Metasurfaces

As two-dimensional embodiments of metamaterials, optical metasurfaces are planar nanophotonic devices composed of spatially varying subwavelength nanostructures that could be designed to control the phase, amplitude, wavelength and polarization of light solely via engineering the geometry and placement of the nanostructures [64-66]. The planar-footprint and subwavelength

thickness of metasurfaces enable their fabrication by using one-step top-down lithography technologies used in mature semiconductor industries, which avoids the challenging manufacturing requirements for resonator based three-dimensional metamaterials and therefore pushing the meta-devices towards practical applications such as optics [67], quantum physics [68-70] and biology [71]. The highly customizable nature of a metasurface allows it to accomplish a variety of functions that have traditionally been fulfilled by a combination of bulk optical elements, such as gratings, lenses, polarizers, wave-plates, beam splitters, and holograms, with a significantly reduced physical size compared to traditional optical elements. Thus far, researchers have demonstrated various types of high-performance metasurfaces performing an array of functionalities such as beam steering [64, 72], high-resolution imaging and display [73-80], hologram projection [81-84], structured light generation [85, 86], asymmetric light transmission [87-89], and temporal pulse shaping [90, 91].

4.1. Working principles of ultraviolet metasurfaces

Following the rapid development of optical metasurfaces over the last decade, they are typically designed using few different fundamental approaches by utilizing: 1) propagation phase [92]; 2) geometric phase [84, 93, 94]; or 3) electromagnetic resonances [64, 95], in the unit-cell choice. The physical principle and applications of metasurfaces from visible wavelengths to microwave wavelengths have been reviewed and summarized in other previous works [96-101]. Due to high photon energy and strong material absorption of UV light [102], it is more challenging to achieve high efficiency in ultraviolet metasurfaces. By introducing novel large-bandgap materials in the design paradigm, we have recently witnessed an exciting development of compact ultraviolet optics, which is highly desired in holography[103], lithography[104], photo-emission spectroscopy[105] and information security[106] applications. For a better understanding, we give a brief review of working principles used in the reported ultraviolet metasurfaces.

4.1.1. Waveguide-based ultraviolet metasurfaces

Waveguide-based metasurfaces usually rely on low-absorption dielectric nanostructures with high refractive index, which enables the formation of a well-defined cavity with low-index background (**Fig. 5a**). Light passing through the dielectric nanostructures propagates through the cavity in a well-confined waveguide mode with its propagation properties dependent on the shapes and size of the nanostructure. If the lateral size of these planar nanostructures is modified, these waveguide

modes oscillate within the nanostructure with a different mode-volume, mode number and field-location (**Fig. 5b**), all of which eventually determine the amplitude and phase of the transmitted light. By optimizing the nanostructures using numerical modelling such as through using the finite-difference-time-domain (FDTD) method or finite-element method (FEM), one can obtain the expected amplitude and phase modulation for the transmitted light. Since such kinds of metasurfaces control light via excitation of waveguide modes, we define them as waveguide-based metasurfaces.

To realize high-efficiency, ultraviolet waveguide-based metasurfaces employ a large bandgap material such as HfO₂ with a bandgap of ≈ 5.7 eV that enables a transparency spectral window down to $\lambda = 217$ nm [103, 107]. Although HfO₂ ($2 < n < 2.5$) has a higher refractive index than quartz or SiO₂ substrate ($n = 1.45$) at the wavelengths of interest, this difference between their indices is small, thus leading to a large volume of the waveguide modes. To guarantee existence of these modes, these waveguide-based metasurfaces in the UV usually require high-aspect-ratio nanopillars to both maximize optical transmission and achieve larger phase depth [74, 108-110]. For example, the nanopillars constituting HfO₂-based waveguide metasurfaces have an aspect ratio ranging from 3 to 10 [103]. Generally, a circular-shape nanopillar is used in waveguide-based metasurfaces, such that the phase modulation can be tailored by only one parameter, the diameter of nanopillar. Due to its circular symmetry, these waveguide-based metasurfaces exhibit no dependence on input polarization, which enables manipulation of light sources with various states of input polarization, or even unpolarized light. To realize high performance, the spacing between two neighboring nanopillars cannot be too small to minimize coupling between waveguide modes of neighboring pillars. Correspondingly, the period of the nanopillars cannot be significantly smaller than the operating wavelength to avoid any coupling effects [111]. This typically results in a design rule-of-thumb of nanopillar period of approximately one half of a wavelength [112], a condition also valid for ultraviolet metasurfaces.

4.1.2. Geometric-phase ultraviolet metasurfaces

Geometric-phase based metasurfaces are composed of anisotropic nanostructures (**Fig. 5c**) that exhibit different responses to two orthogonal electric-field components (i.e., E_x and E_y) of the circularly polarized (CP) incident light [84, 108, 113, 114]. By rotating the nanostructures along a transverse plane, the cross-polarization part of the transmitted or reflected light will immediately harvest a dispersion-free phase that equals twice of the rotation angle. Since this phase is induced

by the geometry operation of the in-plane rotation and operates on both components of the cross-polarized light simultaneously, it is usually described as a geometric phase or Pancharatnam-Berry phase in memory of their pioneer work [115]. To unveil the underlying physics in geometric phase based metasurfaces, we assume that light passing through individual nanostructures have transmission coefficients of t_x and t_y for the E_x and E_y components, respectively. The electric field of CP light has the form of $\mathbf{E}_\sigma = E_0 \cdot [1, \sigma i]^T$, where σ denotes the spin of circular polarization, and T represents the transpose of a matrix. When a nanostructure is rotated by an angle of θ , the vector electric field of transmitted light can be expressed as

$$\begin{aligned} \mathbf{E}_{out} &= E_0 \cdot \mathbf{R}(-\theta) \begin{bmatrix} t_x & 0 \\ 0 & t_y \end{bmatrix} \mathbf{R}(\theta) \begin{bmatrix} 1 \\ \sigma i \end{bmatrix} \\ &= \frac{t_x+t_y}{2} \mathbf{E}_\sigma + \frac{t_x-t_y}{2} e^{2i\sigma\theta} \mathbf{E}_{-\sigma}, \end{aligned} \quad (1)$$

where the rotation operator $\mathbf{R}(\theta) = \begin{bmatrix} \cos\theta & \sin\theta \\ -\sin\theta & \cos\theta \end{bmatrix}$. In eq. (1), one can find that the cross-polarization part in the transmitted light has an additional phase modulation of $2\sigma\theta$, which is independent of the operating wavelength. It indicates that the geometric phase is the result of the interaction between the spin of photons and the geometric coordinate of the objective physical system. The interaction strength is determined by optical anisotropy of the nanostructures, *i.e.*, t_x and t_y .

If $t_x = -t_y = 1$ in eq. (1), the anisotropy is maximized such that the nanostructures work as high-efficiency nanoscale half-waveplates due to the phase delay of π between two orthogonal electric-field components of light. To enhance the optical transmission of nanostructures, it requires co-existence of both electric and magnetic resonances [116], such that the electric and magnetic dipoles have vertical orientation [95]. In dielectric nanostructures, the magnetic dipoles can be induced by a circulating electric displacement current [117]. It has been found that antiferromagnetic modes containing several antiparallel magnetic dipoles (AMDs) usually appear in nanoscale dielectric half waveplates [106]. More importantly, the AMDs induced by the E_x and E_y components have odd and even values, respectively. The electric-field vectors of light at the input and output ends of the nanostructure are reversed for odd AMDs (**Fig. 4d**) but stays the same for even AMDs. It implies that the phase delay is π for E_x but 0 for E_y , thus realizing the functionality of a half-waveplate. Therefore, such antiferromagnetic resonances hold the fundamental mechanism of nanoscale half-waveplates in dielectric geometric metasurfaces. At ultraviolet wavelengths, high-efficiency dielectric geometric-phase based metasurfaces require low-loss materials such as Nb_2O_5

[106] or HfO_2 [103], which have their transparency windows located at wavelengths $\lambda > 340$ nm and $\lambda > 217$ nm, respectively. At even-smaller wavelengths (vacuum ultraviolet and soft x-ray light), all dielectric materials are absorbing [102] hence such antiferromagnetic-resonance-based geometric metasurfaces will not work.

In contrast, the optical anisotropy of a nanostructure is minimum for $t_x = t_y$ that appears in symmetric, circular- and square-shaped, nanostructures. In the transmitted light, the cross-polarization component is zero but the co-polarization part has no geometric phase modulation. It means that circular and square nanostructures cannot be used for geometric-phase based metasurfaces. However, if $t_x \neq t_y$ in eq. (1), the cross-polarization part survives, leading to the possibility of demonstrating geometric-phase based metasurfaces across the entire electromagnetic spectrum. For example, although Si is highly absorbing at ultraviolet wavelengths, a 32 nm wide and 142 nm long Si nanorod was demonstrated to work as a ultraviolet geometric-phase metasurface element from $\lambda = 280$ nm to $\lambda = 400$ nm [104], due to the unequal transmission for E_x and E_y components of light. Even using subwavelength rectangular air-holes etched in a metal film [118], an ultraviolet geometric-phase metasurface has been demonstrated without plasmonic resonances at a wavelength of 355 nm. These results suggest that non-resonant geometric-phase based metasurfaces operating at even shorter wavelengths (such as vacuum ultraviolet, deep ultraviolet, and soft X-ray wavelengths) are feasible in theory only if the nanostructures have an anisotropy in their shape, i.e., they are of different widths and lengths [118]. Due to high intrinsic absorption of light in materials at such short wavelengths, these non-resonant geometric-phase based metasurfaces have extremely low efficiencies, e.g., ≈ 0.4 % reported in one previous work [118]. Furthermore, a customized approach to realize phase control of ultraviolet light has also been proposed by tailoring the density of noble gas [119]. Note that, the non-resonant geometric-phase based metasurfaces work under the condition of subwavelength period of unit cells, implying that the feature size of the employed nanostructures must be much smaller than the operating wavelength. The accompanying fabrication issues to experimentally demonstrate a high-efficiency ultraviolet geometric-phase metasurface is due to the limited patterning resolution of current academic manufacturing technologies. Considering the smallest fabrication feature of several nanometers by using the state-of-the-art industrial equipment and through availability of a low-loss material, the operating wavelength of non-resonant ultraviolet geometric-phase metasurfaces can be scaled down to 10 nm, which is located in the extreme-ultraviolet spectrum.

4.1.3. Resonance-based ultraviolet metasurfaces

Although electromagnetic resonances also exist in waveguide and geometric-phase metasurfaces (**Fig. 5b and 5d**), higher-order modes containing multiple electric or magnetic dipoles are usually observed in those systems. In fact, a nanostructure supporting single electric or magnetic dipole could also be employed to demonstrate ultraviolet metasurfaces. For example, an array of 100 nm tall and 170 nm diameter circular ZnO nanodisks (**Fig. 5e**) is used to induce a magnetic dipole by using circle electric displacement currents at the 395 nm wavelength [120], as shown in **Fig. 5f**. Similarly, toroidal modes considered as non-radiating monopoles can be excited by metallic meta-atoms composed of two mirror-symmetry ‘D’-like nanostructures [37]. Although these two approaches have been demonstrated at ultraviolet wavelengths, other methods, such as single electric dipole resonance [121], or simultaneous excitation of electric and magnetic resonances [95] can also be used for ultraviolet metasurfaces. From the viewpoint of wavefront shaping, a transmissive metasurface based on only single electric or magnetic dipole can only have a maximum phase modulation of π and their efficiency is limited to $< 50\%$ originating from its radiation symmetry [122]. To improve it, both electric and magnetic dipoles oscillating vertically at the transverse plane (perpendicular to the propagation direction of incident light) are needed to exhibit a theoretical maximum transmission of 100% and a full phase modulation of 2π [95]. In this case, due to a lack of backward scattering, every meta-atom or nanostructure behaves like a Huygens point source. Therefore, metasurfaces supporting both electric and magnetic dipoles simultaneously are named as Huygens metasurfaces, and have not been reported yet at ultraviolet wavelengths. Since these metasurfaces only support one or two electromagnetic modes, we call them as resonance-based metasurfaces to discriminate from the waveguide and geometric-phase based metasurfaces. Benefiting from small number of modes, resonance-based metasurfaces have small mode volumes, thereby shrinking their thicknesses down to 100 nm or less, regardless of whether they are based on metallic or dielectric nanostructures.

4.2. Material Platforms and Fabrication of Ultraviolet Metasurfaces

Silicon (Si), a material which is straightforward to deposit and pattern, and therefore typically used for constructing efficient metasurfaces operating in the infrared (IR) and near-IR region [92, 123], has been employed for building devices operating in the UV [104]. In this study, a thin suspended crystalline Si membrane was used to fabricate metasurfaces operating down to the mid-UV and

performing beam bending as well as hologram projection. However, device efficiencies were largely limited by significant absorption loss due to the relatively narrow bandgap of Si ($E_g \approx 1.1$ eV). In order to avoid severe inter-band absorption and realize high-efficiency devices for the UV range, dielectrics of wide bandgap values ($E_g > 3.3$ eV) are preferred as the constituent materials for metasurface fabrication. Representative wide-bandgap dielectric materials include Silicon Dioxide (SiO_2 , $E_g \approx 9.0$ eV), Niobium Pentoxide (Nb_2O_5 , $E_g \approx 3.65$ eV), Hafnium Oxide (HfO_2 , $E_g \approx 5.7$ eV), Aluminum Nitride (AlN , $E_g \approx 6.0$ eV), and Silicon Nitride (Si_3N_4 , $E_g \approx 5.0$ eV). The materials' refractive indices in the UV region are plotted in **Figs. 6a** and **b**. Among them, SiO_2 exhibits the lowest refractive index and is readily obtained in the form of high-quality, large-scale wafers. Therefore, SiO_2 (usually in the form of fused-silica) is typically employed as the substrate material for UV metasurface devices. In purely numerical studies, AlN and Si_3N_4 have been employed to design metalenses operating down to the deep-UV. In experimental works, Nb_2O_5 has been used to construct high-performance devices operating at near-UV wavelengths ($\lambda_0 = 355$ nm) [106]. Moreover, HfO_2 , with an even wider bandgap, has been employed to realize efficient metasurface devices operating down to the record-short deep-UV region [103]. Diamond has also been suggested in theory to shape UV light but without any experimental demonstration because of lack of access to large-scale thin diamond film and the associated fabrication challenges, although diamond has a large bandgap of ≈ 5.5 eV and high refractive index of ≈ 2.4 [124].

One difficulty of implementing wide-bandgap dielectric based UV metasurfaces is fabrication of sub-wavelength-scale, high-aspect-ratio nanostructures. Though directional reactive etching has been demonstrated as a straightforward and effective method to pattern dielectric materials such as Si [90, 92] or GaN [75], the corresponding etching recipes for patterning many of the aforementioned wide-bandgap materials are instead rather underexploited or even impractical. To overcome such limitations, a resist-based Damascene process has been developed. During this process, metasurface patterns are first created in the resist layer by lithography. Then, low-temperature atomic layer deposition (ALD) is utilized to conformally fill in the holes and trenches of the developed resist layer with the targeted wide-bandgap dielectric material. ALD is intentionally performed over a long duration such that all openings of the exposed resist patterns are completely filled, and at the same time, a quasi-planar dielectric layer is formed on top of the resist layer. Following ALD, the overcoated dielectric layer is back-etched to the resist top surface. Finally, the remaining resist is removed, yielding high-aspect-ratio, straight dielectric nanostructures of uniform

height and smooth side-wall profiles (**Figs. 6c and d**). Utilizing such a Damascene process, researchers have successfully implemented Nb₂O₅-based devices operating in the near-UV region and performing hologram projection [106], as well as HfO₂-based devices operating in the near- and deep-UV regions and performing high-numerical-aperture lensing, hologram projection and Airy beam generation [103].

5. Applications

As mentioned above, plasmonic effects have been utilized in metamaterials and metasurfaces for various optical devices. For simplicity of discussion, we only introduce UV devices assisted by the field-enhancement effect of plasmons as well as plasmonic based UV optical elements in Section 5.1. In, addition, considering that metamaterials are difficult to fabricate which has limited its practical applications, we summarize all applications related to UV metamaterials and metasurfaces in Section 5.2, where metalenses, beam steering, holography, photoemission spectroscopy and nonlinear optics are addressed with detailed discussions and summary of important advances.

5.1. Plasmonics-assisted Ultraviolet Devices

The highly confined nature of SPPs result in a strong field enhancement at the interface with air in metal films or at the corners or edges of metallic nanostructures. This field enhancement is extremely helpful for various optical effects that depend on the electric field in a nonlinear manner, e.g., facilitating the observation of photon-created carriers in photodetectors, and increasing the optical field in Raman processes. Here, we introduce the roles of plasmonics in ultraviolet photodetectors and Raman spectroscopy.

5.1.1. Plasmonic Ultraviolet Photodetectors

Photodetectors are important optoelectronic devices that transduce incident photons into excited electrons and holes, to create an electric current [125]. The escaped electrons from the surface of materials must overcome its work function, which is relative to the surface potential. Most ultraviolet photodetectors adopt a large-bandgap material such as GaN as the host material due to its good chemical and thermal stability enabling a longer lifetime of the created hot carriers [125]. Low dark current and high responsivity is the key property for photodetectors, but it is difficult to achieve both of them simultaneously [126]. In addition to temperature dependence, low dark current

needs large work function of materials to decrease the escaping possibility of the thermally excited electrons. However, the large work function also reduces the escape possibility of the photogenerated carriers, thereby leading to low responsivity. Technically, cooling is the most efficient method to suppress dark current and is typically used in various photodetectors.

In comparison, it is desirable to realize high responsivity ultraviolet photodetectors, which will be quite useful for weak-light or single-photon detection for applications in chemistry, quantum optics and astronomy. In addition to the avalanche-type mechanism, high-responsivity ultraviolet photodetectors also employ localized SPPs that provide strong field enhancement [38], which helps to decrease the surface potential of materials around the plasmonic nanoparticles [127]. It decreases the work function and increases the escape possibility of photogenerated electrons, therefore enhancing the responsivity. An ultraviolet photodetector with gold nanoparticles patterned on the surface of GaN (**Fig. 7a**) exhibit ≈ 30 times enhancement in the responsivity than the bare GaN-based detector at the ultraviolet spectrum ranging from $\lambda = 320$ nm to $\lambda = 380$ nm (**Fig. 7b**) [38]. Another AlGaIn-based ultraviolet photodetector with plasmonic effects induced by aluminum nanoparticles has been reported with a two-fold enhancement in the responsivity at wavelengths below 300 nm [128]. More ultraviolet photodetectors on the basis of other mechanisms such as avalanche effects and *p-n* heterojunctions have already been well reviewed in other works [125, 126, 129].

5.1.2. Plasmonic Ultraviolet Surface-Enhancement Raman Scattering

Raman scattering is an inelastic light-matter interaction that enables some of the scattered photons to carry slightly different frequencies determined by optical phonons corresponding to the polarizability of molecules or atoms inside solids or some liquids [130]. The scattering intensity at the Raman frequency depends on the polarizability enhancement and the incident intensity. The polarizability of molecules or atoms is an intrinsic property determined by the chemical bonding for a given material and can be seldom modified by incident photons. In comparison, enhancement of the incident intensity is usually achieved by using the plasmonic resonances at rough surface of metals, which is the underlying physical origin of surface-enhancement Raman scattering (SERS). For a plasmonic surface, the Raman scattering intensity is proportional to the fourth power of the electric-field enhancement factor. Although many SERS spectroscopies have been demonstrated with the silver and gold at the visible and infrared wavelengths, they are not efficient in

characterizing the organic and inorganic molecules with small scattering cross section. Meanwhile, the Raman and fluorescence spectra at the visible and infrared can overlay on top of each other, increasing the background noise of Raman signal. Fortunately, SERS signal under ultraviolet-light excitation can solve these issues due to its high photon energy.

The first ultraviolet SERS was demonstrated with a Raman enhancement of >2 orders of magnitude on rhodium and ruthenium electrodes under 325 nm wavelength excitation [36]. At the same wavelength, enhanced SERS was also reported by using Au electrodes [131]. Although these two pioneering works reported exciting SERS enhancement results, the role of SPPs during the process was not revealed or discussed comprehensively. Meanwhile, the employed metals such as rhodium, ruthenium and gold cannot support deep-ultraviolet plasmon resonances. A better approach by using a thin Al layer for the ultraviolet SERS was reported in 2007 by Popp's group for an excitation wavelength of 245 nm [132], which opens more opportunities for ultraviolet SERS. For example, an Al-coated nanotip under the 266 nm deep-ultraviolet excitation exhibits a Raman enhancement of ≈ 60 to 200 times for various samples such as crystal violet solution and films [133], as shown in **Fig. 7c** and **7d**. In addition, benefitting from resonant Raman effects, caused by the fact that the bandgaps of some DNA and proteins are located at the ultraviolet spectrum, the Raman signal of adenine molecules had an enhancement of ≈ 5 on the top of an Al nanoparticle array [134], compared with the case on the fused silica. Meanwhile, the achieved signal-to-noise ratio of ≈ 50 indicates that the ultraviolet SERS spectroscopy holds the great promise for ultrasensitive detection and characterization of biological issues and molecules.

5.2. Ultraviolet Meta-optics

Due to the challenge of material absorption and fabrication constraints, the development of ultraviolet metasurfaces has only begun since 2018 [37, 104, 120]. Driven by the requirements for industrial applications, ultraviolet metasurfaces have harvested increasing attention due to its compact volume and powerful wavefront shaping capabilities. Novel ultraviolet metadevices have been demonstrated for various applications such as lenses, beam steering, holography, photoemission spectroscopy and nonlinear phenomena. Here, we review the experimental advances of these ultraviolet metadevices.

5.2.1 Metalens

Conventional optical lenses control the wavefront of light through a continuous phase gradient that is accumulated when light propagates through a transparent optical medium having spatially varying thickness. This working principle yields bulky 3D material profiles that are challenging to manufacture within the required wavefront error tolerance, as well as to integrate into compact, miniaturized systems. In contrast, metasurface-based lenses (metalenses) take a radically different approach to achieve the same functionality and output phase profile, which is by using a planar array of phase-shifting elements of sub-wavelength dimensions and spacing [135-137].

HfO₂ has been employed to construct high numerical-aperture (NA = 0.6) metalenses operating at near-UV wavelengths of 364 nm and 325 nm (**Fig. 8a**). The nanoscale building blocks of the UV metalenses consist of high-aspect-ratio HfO₂ circular nanopillars of varying radii arrayed on a fused silica substrate with subwavelength spacing. Each element acts as a truncated dielectric waveguide, through which light propagates with transmission intensity and phase shift controlled by the cylinder height, cylinder radius, and lattice spacing. For the targeted operation wavelength of 364 nm (325 nm), a cylinder height of 550 nm (500 nm), lattice spacing of 200 nm (190 nm), and radius variation range of 50 nm to 160 nm (50 nm to 150 nm) are chosen. For both devices, the measured intensity distribution reveals lensing with a circularly symmetric focal spot, of first-dark-ring diameter close to the theoretical diffraction-limited value (**Figs. 8b and c**). The focusing efficiency, defined as the ratio of the optical power in the focused spot to the total power illuminating the metalens, are $(55.2 \pm 2.6) \%$ (for the 364 nm metalens) and $(56.3 \pm 1.4) \%$ (for the 325 nm metalens). The cited uncertainties represent one standard deviation of the measured data.

5.2.2. Metasurface-based Beam Steering

Traditionally, changing the propagation direction of light can be realized by using optical reflection with a mechanically rotating mirror that is the key element of Galvo scanning systems in optical display projectors, microscopes and LiDAR. Such a traditional mechanical approach is usually bulky, which is not preferred for portable or integrated systems. Although mirrors based on microelectromechanical systems (MEMS) could shrink the length scale to several tens of micrometers, the turning angle for most commercial MEMS mirrors is limited to below $\pm 20^\circ$, which are insufficient in many applications such as large-area imaging or intelligent vehicles. The alternative method for beam steering is to add an additional tilting phase into the incident beam by

using a pure-phase element, such as a spatial light modulator (SLM) [138] or using metasurfaces. The tilting angle is determined by the period of the phase element. The smallest pixel pitch of SLMs is $\approx 3.74 \mu\text{m}$ (Holoeye Gaea), which allows the maximum tilting angle of only a few degrees at the ultraviolet and visible wavelengths. Due to the subwavelength pixel pitch, metasurfaces are one of the promising candidates for large-angle steering. **Fig. 9a** and **9b** sketches Si-based geometric-phase based metasurfaces composed of nanorods with their orientation angle dependent on the location [104]. Within a period of 160 nm, 8 nanorods are used to realize a full-phase modulation of 2π , resulting in a tilting angle of $\pm 13.1^\circ$ at $\lambda = 290 \text{ nm}$ and $\pm 17.3^\circ$ at $\lambda = 380 \text{ nm}$ (**Fig. 9c**). Their experimentally demonstrated efficiency is $\approx 10 \%$ from $\lambda = 280 \text{ nm}$ to $\lambda = 420 \text{ nm}$ (**Fig. 9d**). The tilting angle can be further enlarged by decreasing the number of nanorods in a full phase cycle of 2π , which, however, decreases the efficiency of the tilting beam. Considering the strong absorption of silicon at the ultraviolet spectrum, the upper limit on efficiency is $\approx 10\%$.

HfO₂ with a bandgap of 5.7 eV is a low-loss material platform for the wavefront shaping of light. The waveguide metasurfaces made of circular HfO₂ nanopillars have been reported to create an ultraviolet Airy beam with a cube phase profile that could make the light beam propagate along a curved trajectory without any significant divergence [103], illustrating a non-diffraction feature (**Fig. 9e**). The measured intensity profiles and the experimental trajectories at various wavelengths are shown in **Fig. 9f** and **Fig. 9g**, respectively. Benefiting from the large bandgap, their measured efficiency is $\approx 47 \%$ at $\lambda = 364 \text{ nm}$ and $\approx 67 \%$ at $\lambda = 325 \text{ nm}$, which are the highest efficiency at these selected wavelengths and therefore makes ultraviolet metasurfaces comparable to visible and infrared metasurfaces.

5.2.3. Meta-holography

As another demonstration of wavefront engineering, ultraviolet metasurface holograms have drawn a great deal of attention due to their potential applications in information security and lithography. All reported ultraviolet meta-holograms employ geometric phase that can be easily controlled by the orientation of a fixed-size nanostructure, which facilitates fabrication due to uniformity in nanostructures shape and size. By using semiconductor Nb₂O₅ with a bandgap of $\approx 3.65 \text{ eV}$, an ultraviolet metahologram operating at 355 nm wavelength has been reported with an experimental efficiency of $\approx 79.6 \%$ [106], which is a record-high efficiency for all ultraviolet metasurfaces and metadevices demonstrated till date (**Fig. 10a** and **10b**). Another geometric metahologram by using

HfO₂ nanorods extends the operating spectrum down to $\lambda = 325$ nm and $\lambda = 266$ nm (**Fig. 10c** and **10d**) [103], meanwhile harvesting impressively high efficiency ($\approx (71.8 \pm 2.1)$ % at $\lambda = 325$ nm and $\approx (60.7 \pm 2.6)$ % at $\lambda = 266$ nm). Both works verify that the ultraviolet metasurfaces have a great potential for practical applications because they have solved the efficiency problem. Note that, although both materials Nb₂O₅ and HfO₂ have large bandgap, their refractive indices are ≈ 2 , which is slightly higher than SiO₂ or quartz substrate. It leads to a requirement of high-aspect-ratio nanostructures, e.g., 7 for Nb₂O₅ nanobricks [106] and 3 to 10 for HfO₂ nanorods [103], which are challenging to fabricate via the dry etching process. Therefore, both works utilize the aforementioned electron-beam lithography (EBL) combined with ALD technique to fabricate the metasurfaces.

Ultraviolet geometric-phase based metasurfaces could also realize polarization-multiplexed holograms because the geometric phase is dependent on the handedness of the input circular polarization. A spin-multiplexed metahologram operating at a wavelength of 266 nm is shown to create two spin-dependent images. When left-handed CP light illuminates the metahologram, an image of “deep” is constructed at a distance $z = 40$ mm away from the metasurface (Fresnel region of the metahologram with a size of $330 \mu\text{m} \times 330 \mu\text{m}$), while the right-handed CP light yields the different image of “UV” (**Fig. 10e**) [103]. The phase loaded on the hologram is the weighted super-position of both phase profiles for left- and right-handed CP light, and is used to determine the orientation angle of nanostructures in the meta-hologram. In comparison, another spin-multiplexed ultraviolet metaholograms employs two interleaved apertures [106], each of which encodes two spin-dependent sparse holograms (**Fig. 10f**). One sparse metahologram for left-handedness CP light reconstructs an image of “girl” pattern at the Fresnel region, while the other hologram for right-handedness CP light creates the complementary “snake” pattern. Both “girl” and “snake” patterns are complementary to each other so that their combined pattern is observed as another image of “trophy”. Thus, one can directly see a picture of “trophy” under linearly polarized illumination. After the polarization analysis, the pattern “trophy” exhibits a vector feature (**Fig. 10g**), which can provide an additional degree of freedom for the purpose of optical anticounterfeiting. It is attributed to the spin multiplexing functionality of geometric metasurfaces. Note that both spin-multiplexing approaches realize the holographic reconstruction at the Fresnel region, where the image is real for one spin but becomes virtual for the reversed spin [93, 139]. In contrast, the

Fraunhofer metaholograms have center-symmetric real images for both spins [140]. A united mathematical explanation has been given in a newly published book [141].

In addition to optical anticounterfeiting, ultraviolet metaholograms has also been used for optical lithography because high energy of ultraviolet photons can help to break chemical bonds of molecules in some photoresists such as polymethyl methacrylate (PMMA) and Hydrogen silsesquioxane (HSQ). An ultrathin (40 nm thickness) Si metahologram operating at $\lambda = 380$ nm creates the image “Cal”, which is used to expose the photoresist [104]. The experimental results are shown in **Fig. 10h**, which indicates good performance. Considering the interference speckles created in the holographic image, a dynamic random phase provided by a rotating optical diffuser is used to increase the coherence of the diffracted light, thus enhancing the homogeneity of the image. From the viewpoint of optical performance, speckle is one of the main issues for the holography-based lithography. Except the dynamic random phase, one might remove the holography speckles by using a broadband laser source, or utilize advanced design of hologram phase via artificial intelligence technology. Reconfigurability of ultraviolet metasurfaces is another challenging problem for metaholography-based lithography [142].

5.2.4. Photoemission spectroscopy by ultraviolet flat optics

The high-energy photons of ultraviolet light could excite electron emission from materials, and is named as the photoelectric effect and discovered by Heinrich Hertz in 1887. By collecting the emitted electrons at the different angles, the electronic structure of solids can be probed by measuring the energy and momentum of the emitted electrons, which holds for the working principle of angle-resolved photoemission spectroscopy (ARPES) as a powerful tool for characterization of materials [143]. Traditional ARPES utilizes x-ray light which is typically generated at expensive synchrotron radiation facilities. In addition, x-ray-based ARPES has various drawbacks such as low energy resolution and bulky volume, which stimulated the invention of vacuum-ultraviolet-laser based ARPES. Since the first development of laser ARPES in 2008 [144], several kinds of laser ARPES have been demonstrated at different laser wavelengths [145, 146]. The typical laser spots in these systems is >3 μm , and therefore cannot satisfy the rapidly increasing requirement for characterizing micrometer-sized quantum materials, or two-dimensional materials. Very recently, a novel spherical-aberration-free zone-plate-based flat lens has been proposed to focus a 177 nm laser into a sub-micrometer spot of ≈ 0.8 μm (**Fig. 11a-11c**) [105], which is the first demonstration of sub-

micrometer resolved laser ARPES. Using this spot, various samples such as metallic gratings, graphene flakes are characterized with sub-micrometer resolution (**Fig. 11d and 11e**). Although these zone plates are made of metallic materials for blocking light without electromagnetic resonances, they are categorized as the amplitude-type ultraviolet nano-devices, hereby within the scope of this review. In fact, at vacuum ultraviolet spectrum and beyond, absorption is the dominant electromagnetic loss mechanism and there are no transparent materials with high refractive index for development of these resonance-based metasurfaces. Thus, photonic platforms such as zone plates [112, 147-150] and nanosieves [151-155] are good candidates for ultraviolet nano-devices. However, these platforms work by manipulating ultraviolet light's diffraction from the structures, where the strong diffraction (relative to the large ratio of the operating wavelength to the feature size of the structures) is a mandatory requirement for maintaining high optical performance of these devices. In addition, the diffraction of ultraviolet light also determines the efficiency of the entire device, and hence the structures for ultraviolet-light manipulation is extremely important.

5.2.5. Nonlinear meta-optics

As discussed above, nanostructures in metasurfaces could confine or induce electromagnetic resonance modes. Due to their subwavelength feature size, the electric fields within or near the nanostructures are much higher than the incident light, thus enhancing the light-matter interaction at ultraviolet wavelengths. Such a phenomenon has a direct application in creating ultraviolet light source through nonlinear processes, where the transfer efficiency of nonlinear signals is proportional to the intensity of the electric-field inside the nonlinear material. Categorized by the location of the induced optical modes, the reported works pursue two approaches (direct and indirect) to realize the creation of ultraviolet light.

The direct method is to use low-loss ZnO nanodisks for the confinement of a magnetic dipole induced by a circular electric displacement current (**Fig. 12a**), such that the pumped 394 nm femtosecond laser is trapped inside the nanostructures [120], with a transmission of nearly zero. Thus, the trapped optical modes interact with the second order nonlinearity of ZnO leading to second harmonic generation at 197 nm (**Fig. 12b**). Meanwhile, due to the low absorption, these modes have long lifetime and therefore enable multiple resonances inside the nanostructures, eventually enhancing the nonlinear interactions. Alternatively, a better confinement of optical modes is achieved by employing bound states in the continuum (BIC), where the eigenmodes are localized in

the nanostructures with a continuous spectrum of the radiating waves [156]. Due to a much narrower bandwidth, BICs have a longer lifetime and therefore should behave better for the generation of nonlinear signals, which, however, has not been demonstrated in experiment because BICs also need high reciprocity between both sides of the sample [157].

The other approach leverages an indirect interaction between a third material such as ITO and the induced confined optical modes that exist outside the metallic nanostructures. As shown in **Fig. 12c**, the meta-atoms contain two “D”-like nanostructures that support the toroidal dipole resonance under the illumination of a linearly polarized light [37]. The toroidal dipole having a charge-current configuration exhibits strong electromagnetic localization, which can be used to enhance the nonlinear signals of the underlying ITO film. Under illumination with 785 nm wavelength fundamental laser, its third harmonic generation (THG) signals at 262 nm wavelength is ≈ 2.2 times greater than that of the disk-dimer array, verifying the validity of the toroidal-dipole resonances (**Fig. 12d**). In addition to enhancement of nonlinear signals, these dielectric metasurfaces with high-quality-factor nano-resonators can also be used to demonstrate ultraviolet circular dichroism [158].

6. Outlook and Conclusion

Although ultraviolet nanophotonics has progressed rapidly through developments in various fields such as plasmonics, metamaterials, and metasurfaces over the past two decades, some fundamental challenges still exist which has prevented UV nanophotonics from being widely employed for industrial applications. To pursue a better solution, we highlight some of these challenges below:

(i) UV-light sources are less developed with the intractable problems such as limited wavelengths, bad tunability, low output power and high cost (compared with visible and infrared lasers). Therefore, nonlinear process by pumping a nonlinear crystal with ultrafast laser is usually used to create the expected UV light [104], which, however, has usually bad coherence lengths and low power, making them non-ideal for field applications. Another choice to obtain high-brightness, monochromatic and highly collimated UV light with even-shorter wavelengths is through synchrotron radiation sources, which are extremely high cost, bulky and only available at a very limited number of institutions worldwide.

(ii) Strong absorption of UV light limits the choice of materials to develop high-performance UV optical elements such as aberration-free lenses, high-transmission and ultrabroadband polarizers and

waveplates. This material issue has severe influence on UV nanophotonics that leverages electromagnetic responses based solely on electric and magnetic dipoles or multipoles, which further increase the loss of UV light. Moreover, to achieve the desired electromagnetic resonances, nanostructures in UV metasurfaces must have high refractive index and low absorption loss simultaneously, which are quite challenging to obtain for most natural occurring materials.

(iii) Challenges in fabrication become serious for shorter-wavelength UV nanophotonics. As the wavelength scales down, the feature size of the nanostructures in the nano-devices must concurrently shrink, which has a two-fold influence on fabrication. The first is increasingly limited tolerance for a given fabrication error, and the other is that small features of nanostructures will eventually reach the limit of fabrication and cannot be realized experimentally. The current fabrication limits are ≈ 10 nm for electron-beam lithography [159], ≈ 50 nm for focused Ga-ion beam lithography [148], and ≈ 5 nm for focused Helium-ion beam lithography [160].

(iv) Detecting UV light efficiently is another challenge because of the low quantum efficiency for most UV detectors such as Complementary Metal Oxide Semiconductor (CMOS) and charge-coupled device (CCD) cameras. Most Si or GaN-based photodetectors have a quantum efficiency of $< 30\%$ in the near-UV range [161] and even smaller at shorter wavelengths. This is caused by quite shallow penetration depth of UV photons inside the material of photodetectors due to strong absorption. Although amorphous-Se based photodetectors have been reported with quantum efficiency more than 1000% at some special wavelengths [162, 163], any mature commercial products with high quantum efficiency over a broadband UV spectrum are still unavailable.

(v) High photon energy of UV light not only can break chemical bonds of materials for photocatalysis in chemistry [164, 165], but also does an irreversible damage to the structures of molecules and cells in biology [166]. Therefore, another challenge is to determine the best mechanism to introduce UV light into various multidisciplinary fields in a safe way. For example, because of the irreversible damage to living organisms, UV light can work as a powerful tool to kill various viruses and bacteria in public hospitals, vehicles, schools, etc., but it can also be carcinogenic and harmful to humans.

These challenges exist in the entire UV industry, and are not just limited to UV optics and nanophotonics. Considering the fact that traditional elements manipulate UV light via refraction and reflection for various functional devices, the emerging UV nanophotonics is a real game changer, because it shapes UV light via diffraction at a subwavelength scale and can arbitrarily manipulate

UV optics with advantages of dense integration, multi-functionality, wavelength multiplexing, light weight and planar CMOS compatible fabrication. Together these advantages open unprecedented opportunities for next-generation UV optics and might offer possible solutions to many of these ongoing challenges. Based on our previous knowledge and understanding of UV nanophotonics, we outline some potential future research directions.

First, developing new low-absorption materials for UV light is a long-term and persistent task. Synthesizing novel inorganic or organic compound that might provide unexplored and large bandgap structures for UV-light manipulation. Patterning artificial structures with few-nanometer feature size into a commonly used UV material or crystal [148] might modify optical responses of microscopic quasi-particles, such as acoustic and optical phonons, polaritons, excitons and orbitons, due to the redistributed density of electrons in material. A similar but different chemical method by selectively etching of target atoms and maintaining the others, named as “nanomesh” in chemistry [167, 168], is a good example to create a new material with distinct and unexplored electronic and optical properties. New UV materials will promote the development of UV elements, devices and systems, as well as the investigation of UV lasers or diodes.

Second, the reported UV plasmonic and metasurface devices, such as lens, hologram, beam splitter, are still insufficient for boosting academic research and industrial applications relying on UV. Many important elements including waveplates, filters, polarizers, high-numerical-aperture and aberration-free flat lenses, commercial UV detectors with high quantum efficiency, have not been demonstrated. This is another future direction that must be pursued in order to substitute or compliment traditional bulk optics technology. Meanwhile, another possible engineering issue is to miniaturize the current UV bulky systems and lasers, which might enable portable UV products such as currency detectors and UV disinfection lighting devices.

Furthermore, UV nanophotonics at the even-shorter wavelengths such as extreme UV, vacuum UV and soft-X ray does not exist due to the lack of commonly used optical elements. However, their extremely small wavelengths allow light-matter interaction with much higher precision for various applications in nuclear physics, semiconductor lithography and material analysis. Therefore, it is expected that VUV and EUV nanophotonics will be the future once the auxiliary optics can be easily obtained.

Finally, searching for new applications in multidisciplinary fields is one future goal of the UV industry. The already developed applications should be improved further, for example, high-

efficiency and ultra-broadband UV metalenses with the intriguing properties including sub-diffraction-limit focusing and imaging, increasing the security level of UV holography by using more degrees of freedom for the purpose of information coding and anticounterfeiting, suppressing the focusing spot of UV light in photoemission spectroscopy down to 100 nm that is comparable to that of x-ray-based ARPES, developing novel nanostructures with stronger nonlinear responses via emerging physical mechanisms such as bound states in the continuum[169], epsilon-zero materials[170], and Moire lattices[171]. New applications of UV nanophotonics might occur if it links communication [172], photocatalysis [164, 165], optogenetics [173] and oxidation [174]. In addition, taking into account that the bandgaps of DNAs and proteins are located at the UV spectrum [175], the UV-nanophotonics-based bio-sensor and bio-detection might become the next exciting application in combination with Raman scattering, nonlinear harmonic generation or photoluminescence.

In conclusion, we have given a brief introduction and overview of ultraviolet nanophotonics. The recent advances in ultraviolet plasmonics, metamaterials and metasurfaces have been reviewed along with discussions of their physical origins, unique properties, existing problems, and demonstrated applications. The challenges of efficient and bright light sources, material absorption, device fabrication, light detection and correct usage in practical applications are discussed in detail with the hope of a solution in the near future. The prospects of future research directions and unsolved problems has been provided on the basis of our best knowledge of the field of ultraviolet optics and nanophotonics. Although UV nanophotonics has gained increasing attention with exciting achievements recently, it is still at its infancy in both scientific research and industrial applications and therefore it is expected to develop further in the future due to their many-fold advantages in light-mater interaction.

Acknowledgements

K.H. thanks CAS Pioneer Hundred Talents Program, “the Fundamental Research Funds for the Central Universities” in China, USTC Research Funds of the Double First-Class Initiative (Grant No. YD2030002003), the National Natural Science Foundation of China (Grant No. 61875181 and 61705085), and the support from the University of Science and Technology of China’s Centre for Micro and Nanoscale Research and Fabrication. C.Z. and Z.L. acknowledge the startup funding from the Huazhong University of Science and Technology and support from the National Natural

Science Foundation of China (Grant No. 62075078). W.Z. and A.A. acknowledge support under the Cooperative Research Agreement between the University of Maryland and the National Institute of Standards and Technology Physical Measurement Laboratory, Award No. 70NANB14H209, through the University of Maryland.

References

- [1] J. Barth, "Johann Wilhelm Ritter (1776-1810) and the discovery of ultraviolet irradiation 185 years ago," *Der Hautarzt; Zeitschrift fur Dermatologie, Venerologie, und verwandte Gebiete*, vol. 38, pp. 301-303, 1987.
- [2] M. S. Shur and R. Gaska, "Deep-Ultraviolet Light-Emitting Diodes," *IEEE Trans. Electron Devices*, vol. 57, pp. 12-25, 2010.
- [3] A. Khan, K. Balakrishnan and T. Katona, "Ultraviolet light-emitting diodes based on group three nitrides," *Nat. Photonics*, vol. 2, pp. 77-84, 2008.
- [4] K. H. Li, X. Liu, Q. Wang, et al., "Ultralow-threshold electrically injected AlGaN nanowire ultraviolet lasers on Si operating at low temperature," *Nat. Nanotechnol.*, vol. 10, pp. 140-144, 2015.
- [5] H. Wu, H. Yu, Z. Yang, et al., "Designing a Deep-Ultraviolet Nonlinear Optical Material with a Large Second Harmonic Generation Response," *J. Am. Chem. Soc.*, vol. 135, pp. 4215-4218, 2013.
- [6] T. T. Luu, Z. Yin, A. Jain, et al., "Extreme-ultraviolet high-harmonic generation in liquids," *Nat. Commun.*, vol. 9, p. 3723, 2018.
- [7] S. Ghimire, A. D. DiChiara, E. Sistrunk, et al., "Observation of high-order harmonic generation in a bulk crystal," *Nat. Phys.*, vol. 7, pp. 138-141, 2011.
- [8] Y. Yang, J. Lu, A. Manjavacas, et al., "High-harmonic generation from an epsilon-near-zero material," *Nat. Phys.*, vol. 15, pp. 1022-1026, 2019.
- [9] B. Wu, D. Tang, N. Ye, et al., "Linear and nonlinear optical properties of the KBe₂BO₃F₂ (KBBF) crystal," *Opt. Mater.*, vol. 5, pp. 105-109, 1996.
- [10] G. Zou, N. Ye, L. Huang, et al., "Alkaline-alkaline earth fluoride carbonate crystals ABCO₃F (A= K, Rb, Cs; B= Ca, Sr, Ba) as nonlinear optical materials," *J. Am. Chem. Soc.*, vol. 133, pp. 20001-20007, 2011.
- [11] R. Schupp, F. Torretti, R. Meijer, et al., "Efficient generation of extreme ultraviolet light from Nd: YAG-driven microdroplet-tin plasma," *Phys. Rev. Appl.*, vol. 12, p. 014010, 2019.
- [12] T. Shintake, H. Tanaka, T. Hara, et al., "A compact free-electron laser for generating coherent radiation in the extreme ultraviolet region," *Nat. Photonics*, vol. 2, pp. 555-559, 2008.
- [13] N. J. Greenfield, "Using circular dichroism spectra to estimate protein secondary structure," *Nat. Protoc.*, vol. 1, pp. 2876-2890, 2006.
- [14] M. Oppermann, B. Bauer, T. Rossi, et al., "Ultrafast broadband circular dichroism in the deep ultraviolet," *Optica*, vol. 6, pp. 56-60, 2019.
- [15] B. Ranjbar and P. Gill, "Circular Dichroism Techniques: Biomolecular and Nanostructural Analyses-A Review," *Chem. Biol. Drug Des.*, vol. 74, pp. 101-120, 2009.
- [16] A. O. Nwokeoji, P. M. Kilby, D. E. Portwood, et al., "Accurate Quantification of Nucleic Acids Using Hypochromicity Measurements in Conjunction with UV Spectrophotometry," *Anal. Chem.*, vol. 89, pp. 13567-13574, 2017.
- [17] A. Dell'Anno, M. Fabiano, G. C. A. Duineveld, et al., "Nucleic Acid (DNA, RNA) Quantification and RNA/DNA Ratio Determination in Marine Sediments: Comparison of Spectrophotometric,

- Fluorometric, and HighPerformance Liquid Chromatography Methods and Estimation of Detrital DNA," *Appl. Environ. Microbiol.*, vol. 64, pp. 3238-3245, 1998.
- [18] R. H. Stulen and D. W. Sweeney, "Extreme ultraviolet lithography," *IEEE J. Quantum Electron.*, vol. 35, pp. 694-699, 1999.
- [19] B. Wu and A. Kumar, "Extreme ultraviolet lithography: A review," *Journal of Vacuum Science & Technology B: Microelectronics and Nanometer Structures Processing, Measurement, and Phenomena*, vol. 25, pp. 1743-1761, 2007.
- [20] M. Heßling, K. Hönes, P. Vatter, et al., "Ultraviolet irradiation doses for coronavirus inactivation - review and analysis of coronavirus photoinactivation studies," *GMS hygiene and infection control*, vol. 15, p. Doc08, 2020.
- [21] T. Bintsis, E. Litopoulou-Tzanetaki and R. K. Robinson, "Existing and potential applications of ultraviolet light in the food industry – a critical review," *J. Sci. Food Agric.*, vol. 80, pp. 637-645, 2000.
- [22] Y. Kivshar, "All-dielectric meta-optics and non-linear nanophotonics," *Natl. Sci. Rev.*, vol. 5, pp. 144-158, 2018.
- [23] M. Pu, X. Ma, X. Li, et al., "Merging plasmonics and metamaterials by two-dimensional subwavelength structures," *J. Mater. Chem. C*, vol. 5, pp. 4361-4378, 2017.
- [24] A. M. Urbas, Z. Jacob, L. D. Negro, et al., "Roadmap on optical metamaterials," *J. Opt.*, vol. 18, p. 093005, 2016.
- [25] K. Yao and Y. Liu, "Plasmonic metamaterials," *Nanotechnol. Rev.*, vol. 3, pp. 177-210, 2014.
- [26] X. Luo, "Engineering Optics 2.0: A Revolution in Optical Materials, Devices, and Systems," *ACS Photonics*, vol. 5, pp. 4724-4738, 2018.
- [27] Y. Liu and X. Zhang, "Metamaterials: a new frontier of science and technology," *Chem. Soc. Rev.*, vol. 40, pp. 2494-2507, 2011.
- [28] A. Karabchevsky, A. Katiyi, A. S. Ang, et al., "On-chip nanophotonics and future challenges," *Nanophotonics*, vol. 9, pp. 3733-3753, 2020.
- [29] S. A. Maier, *Plasmonics: fundamentals and applications*. Springer Science & Business Media: 2007.
- [30] A. V. Zayats, I. I. Smolyaninov and A. A. Maradudin, "Nano-optics of surface plasmon polaritons," *Physics Reports*, vol. 408, pp. 131-314, 2005.
- [31] C. Langhammer, M. Schwind, B. Kasemo, et al., "Localized Surface Plasmon Resonances in Aluminum Nanodisks," *Nano Lett.*, vol. 8, pp. 1461-1471, 2008.
- [32] J. M. McMahon, G. C. Schatz and S. K. Gray, "Plasmonics in the ultraviolet with the poor metals Al, Ga, In, Sn, Tl, Pb, and Bi," *Phys. Chem. Chem. Phys.*, vol. 15, pp. 5415-5423, 2013.
- [33] P. Shekhar, S. Pendharker, H. Sahasrabudhe, et al., "Extreme ultraviolet plasmonics and Cherenkov radiation in silicon," *Optica*, vol. 5, pp. 1590-1596, 2018.
- [34] Z. Dong, T. Wang, X. Chi, et al., "Ultraviolet Interband Plasmonics With Si Nanostructures," *Nano Lett.*, vol. 19, pp. 8040-8048, 2019.
- [35] J. B. Khurgin, "How to deal with the loss in plasmonics and metamaterials," *Nat. Nanotechnol.*, vol. 10, pp. 2-6, 2015.
- [36] B. Ren, X. F. Lin, Z. L. Yang, et al., "Surface-enhanced Raman scattering in the ultraviolet spectral region: UV-SERS on rhodium and ruthenium electrodes," *J. Am. Chem. Soc.*, vol. 125, pp. 9598-9, 2003.
- [37] A. Ahmadivand, M. Semmlinger, L. Dong, et al., "Toroidal dipole-enhanced third harmonic generation of deep ultraviolet light using plasmonic meta-atoms," *Nano Lett.*, vol. 19, pp. 605-611, 2018.
- [38] D. Li, X. Sun, H. Song, et al., "Realization of a High-Performance GaN UV Detector by Nanoplasmonic Enhancement," *Adv. Mater.*, vol. 24, pp. 845-849, 2012.
- [39] I. Gryczynski, J. Malicka, Z. Gryczynski, et al., "Ultraviolet Surface Plasmon-Coupled Emission Using Thin Aluminum Films," *Anal. Chem.*, vol. 76, pp. 4076-4081, 2004.

- [40] F. J. García de Abajo, "Optical excitations in electron microscopy," *Rev. Mod. Phys.*, vol. 82, pp. 209-275, 2010.
- [41] M. W. Knight, L. Liu, Y. Wang, et al., "Aluminum plasmonic nanoantennas," *Nano Lett.*, vol. 12, pp. 6000-6004, 2012.
- [42] V. G. Veselago, "THE ELECTRODYNAMICS OF SUBSTANCES WITH SIMULTANEOUSLY NEGATIVE VALUES OF ϵ AND μ ," *Soviet Physics Uspekhi*, vol. 10, pp. 509-514, 1968.
- [43] S. Xi, H. Chen, T. Jiang, et al., "Experimental Verification of Reversed Cherenkov Radiation in Left-Handed Metamaterial," *Phys. Rev. Lett.*, vol. 103, p. 194801, 2009.
- [44] R. A. Shelby, D. R. Smith and S. Schultz, "Experimental Verification of a Negative Index of Refraction," *Science*, vol. 292, pp. 77-79, 2001.
- [45] J. B. Pendry, "Negative refraction makes a perfect lens," *Phys. Rev. Lett.*, vol. 85, p. 3966, 2000.
- [46] D. Ye, K. Chang, L. Ran, et al., "Microwave gain medium with negative refractive index," *Nat. Commun.*, vol. 5, p. 5841, 2014.
- [47] V. M. Shalaev, "Optical negative-index metamaterials," *Nat. Photonics*, vol. 1, pp. 41-48, 2007.
- [48] H. J. Lezec, J. A. Dionne and H. A. Atwater, "Negative Refraction at Visible Frequencies," *Science*, vol. 316, pp. 430-432, 2007.
- [49] E. Verhagen, R. de Waele, L. Kuipers, et al., "Three-Dimensional Negative Index of Refraction at Optical Frequencies by Coupling Plasmonic Waveguides," *Phys. Rev. Lett.*, vol. 105, p. 223901, 2010.
- [50] T. Xu, A. Agrawal, M. Abashin, et al., "All-angle negative refraction and active flat lensing of ultraviolet light," *Nature*, vol. 497, pp. 470-474, 2013.
- [51] A. Poddubny, I. Iorsh, P. Belov, et al., "Hyperbolic metamaterials," *Nat. Photonics*, vol. 7, pp. 948-957, 2013.
- [52] C. Zhang, N. Hong, C. Ji, et al., "Robust Extraction of Hyperbolic Metamaterial Permittivity Using Total Internal Reflection Ellipsometry," *ACS Photonics*, vol. 5, pp. 2234-2242, 2018.
- [53] P. Shekhar, J. Atkinson and Z. Jacob, "Hyperbolic metamaterials: fundamentals and applications," *Nano Convergence*, vol. 1, p. 14, 2014.
- [54] X. Yang, J. Yao, J. Rho, et al., "Experimental realization of three-dimensional indefinite cavities at the nanoscale with anomalous scaling laws," *Nat. Photonics*, vol. 6, pp. 450-454, 2012.
- [55] H. N. S. Krishnamoorthy, Z. Jacob, E. Narimanov, et al., "Topological Transitions in Metamaterials," *Science*, vol. 336, pp. 205-209, 2012.
- [56] D. Lu, J. J. Kan, E. E. Fullerton, et al., "Enhancing spontaneous emission rates of molecules using nanopatterned multilayer hyperbolic metamaterials," *Nat. Nanotechnol.*, vol. 9, pp. 48-53, 2014.
- [57] K.-C. Shen, C.-T. Ku, C. Hsieh, et al., "Deep-Ultraviolet Hyperbolic Metacavity Laser," *Adv. Mater.*, vol. 30, p. 1706918, 2018.
- [58] Y. Guo, C. L. Cortes, S. Molesky, et al., "Broadband super-Planckian thermal emission from hyperbolic metamaterials," *Appl. Phys. Lett.*, vol. 101, p. 131106, 2012.
- [59] P. N. Dyachenko, S. Molesky, A. Y. Petrov, et al., "Controlling thermal emission with refractory epsilon-near-zero metamaterials via topological transitions," *Nat. Commun.*, vol. 7, p. 11809, 2016.
- [60] T. U. Tumkur, L. Gu, J. K. Kitur, et al., "Control of absorption with hyperbolic metamaterials," *Appl. Phys. Lett.*, vol. 100, p. 161103, 2012.
- [61] Z. Liu, H. Lee, Y. Xiong, et al., "Far-Field Optical Hyperlens Magnifying Sub-Diffraction-Limited Objects," *Science*, vol. 315, pp. 1686-1686, 2007.
- [62] X. Chen, C. Zhang, F. Yang, et al., "Plasmonic Lithography Utilizing Epsilon Near Zero Hyperbolic Metamaterial," *ACS Nano*, vol. 11, pp. 9863-9868, 2017.
- [63] T. Xu and H. J. Lezec, "Visible-frequency asymmetric transmission devices incorporating a hyperbolic metamaterial," *Nat. Commun.*, vol. 5, p. 4141, 2014.
- [64] N. Yu, P. Genevet, M. A. Kats, et al., "Light propagation with phase discontinuities: generalized laws of reflection and refraction," *Science*, vol. 334, pp. 333-337, 2011.

- [65] P. Lalanne, S. Astilean, P. Chavel, et al., "Blazed binary subwavelength gratings with efficiencies larger than those of conventional échelette gratings," *Opt. Lett.*, vol. 23, pp. 1081-1083, 1998.
- [66] Z. Bomzon, G. Biener, V. Kleiner, et al., "Spatial Fourier-transform polarimetry using space-variant subwavelength metal-stripe polarizers," *Opt. Lett.*, vol. 26, pp. 1711-1713, 2001.
- [67] K. Huang, D. Zhao, F. Tjioharsono, et al., "Bio-inspired Photonic Masquerade with Perturbative Metasurfaces," *ACS Nano*, vol. 14, pp. 7529-7537, 2020.
- [68] K. Huang, H. Liu, S. Restuccia, et al., "Spiniform phase-encoded metagratings entangling arbitrary rational-order orbital angular momentum," *Light: Sci. Appl.*, vol. 7, p. 17156, 2018.
- [69] T. Stav, A. Faerman, E. Maguid, et al., "Quantum entanglement of the spin and orbital angular momentum of photons using metamaterials," *Science*, vol. 361, pp. 1101-1104, 2018.
- [70] K. Wang, J. G. Titchener, S. S. Kruk, et al., "Quantum metasurface for multiphoton interference and state reconstruction," *Science*, vol. 361, pp. 1104-1108, 2018.
- [71] F. Yesilkoy, E. R. Arvelo, Y. Jahani, et al., "Ultrasensitive hyperspectral imaging and biodetection enabled by dielectric metasurfaces," *Nat. Photonics*, vol. 13, pp. 390 – 396, 2019.
- [72] D. Lin, M. Melli, E. Poliakov, et al., "Optical metasurfaces for high angle steering at visible wavelengths," *Sci. Rep.*, vol. 7, p. 2286, 2017.
- [73] T. Phan, D. Sell, E. W. Wang, et al., "High-efficiency, large-area, topology-optimized metasurfaces," *Light: Sci. Appl.*, vol. 8, p. 48, 2019.
- [74] M. Khorasaninejad, W. T. Chen, R. C. Devlin, et al., "Metalenses at visible wavelengths: Diffraction-limited focusing and subwavelength resolution imaging," *Science*, vol. 352, pp. 1190-1194, 2016.
- [75] R. J. Lin, V.-C. Su, S. Wang, et al., "Achromatic metalens array for full-colour light-field imaging," *Nat. Nanotechnol.*, vol. 14, pp. 227-231, 2019.
- [76] W. Yang, S. Xiao, Q. Song, et al., "All-dielectric metasurface for high-performance structural color," *Nat. Commun.*, vol. 11, p. 1864, 2020.
- [77] S. Sun, Z. Zhou, C. Zhang, et al., "All-Dielectric Full-Color Printing with TiO₂ Metasurfaces," *ACS Nano*, vol. 11, pp. 4445-4452, 2017.
- [78] B. Yang, W. Liu, Z. Li, et al., "Ultrahighly Saturated Structural Colors Enhanced by Multipolar-Modulated Metasurfaces," *Nano Lett.*, vol. 19, pp. 4221-4228, 2019.
- [79] W.-J. Joo, J. Kyoung, M. Esfandyarpour, et al., "Metasurface-driven OLED displays beyond 10,000 pixels per inch," *Science*, vol. 370, pp. 459-463, 2020.
- [80] Y.-K. R. Wu, A. E. Hollowell, C. Zhang, et al., "Angle-Insensitive Structural Colours based on Metallic Nanocavities and Coloured Pixels beyond the Diffraction Limit," *Sci. Rep.*, vol. 3, p. 1194, 2013.
- [81] L. Huang, S. Zhang and T. Zentgraf, "Metasurface holography: from fundamentals to applications," *Nanophotonics*, vol. 7, pp. 1169-1190, 2018.
- [82] A. C. Overvig, S. Shrestha, S. C. Malek, et al., "Dielectric metasurfaces for complete and independent control of the optical amplitude and phase," *Light: Sci. Appl.*, vol. 8, p. 92, 2019.
- [83] Q. Fan, M. Liu, C. Zhang, et al., "Independent Amplitude Control of Arbitrary Orthogonal States of Polarization via Dielectric Metasurfaces," *Phys. Rev. Lett.*, vol. 125, p. 267402, 2020.
- [84] G. Zheng, H. Mühlenbernd, M. Kenney, et al., "Metasurface holograms reaching 80% efficiency," *Nat. Nanotechnol.*, vol. 10, pp. 308-312, 2015.
- [85] Q. Fan, W. Zhu, Y. Liang, et al., "Broadband Generation of Photonic Spin-Controlled Arbitrary Accelerating Light Beams in the Visible," *Nano Lett.*, vol. 19, pp. 1158-1165, 2019.
- [86] W. T. Chen, M. Khorasaninejad, A. Y. Zhu, et al., "Generation of wavelength-independent subwavelength Bessel beams using metasurfaces," *Light: Sci. Appl.*, vol. 6, pp. e16259-e16259, 2017.
- [87] C. Zhang, C. Pfeiffer, T. Jang, et al., "Breaking Malus' law: Highly efficient, broadband, and angular robust asymmetric light transmitting metasurface," *Laser Photonics Rev.*, vol. 10, pp. 791-798, 2016.

- [88] K. Chen, G. Ding, G. Hu, et al., "Directional Janus Metasurface," *Adv. Mater.*, vol. 32, p. 1906352, 2020.
- [89] D. Ma, Z. Li, Y. Zhang, et al., "Giant spin-selective asymmetric transmission in multipolar-modulated metasurfaces," *Opt. Lett.*, vol. 44, pp. 3805-3808, 2019.
- [90] S. Divitt, W. Zhu, C. Zhang, et al., "Ultrafast optical pulse shaping using dielectric metasurfaces," *Science*, vol. 364, pp. 890-894, 2019.
- [91] A. M. Shaltout, K. G. Lagoudakis, J. van de Groep, et al., "Spatiotemporal light control with frequency-gradient metasurfaces," *Science*, vol. 365, pp. 374-377, 2019.
- [92] A. Arbabi, Y. Horie, M. Bagheri, et al., "Dielectric metasurfaces for complete control of phase and polarization with subwavelength spatial resolution and high transmission," *Nat. Nanotechnol.*, vol. 10, pp. 937-943, 2015.
- [93] K. Huang, Z. Dong, S. Mei, et al., "Silicon multi - meta - holograms for the broadband visible light," *Laser Photonics Rev.*, vol. 10, pp. 500-509, 2016.
- [94] E. Hasman, V. Kleiner, G. Biener, et al., "Polarization dependent focusing lens by use of quantized Pancharatnam–Berry phase diffractive optics," *Appl. Phys. Lett.*, vol. 82, pp. 328-330, 2003.
- [95] M. Decker, I. Staude, M. Falkner, et al., "High-Efficiency Dielectric Huygens' Surfaces," *Adv. Opt. Mater.*, vol. 3, pp. 813-820, 2015.
- [96] L. Zhang, S. Mei, K. Huang, et al., "Advances in Full Control of Electromagnetic Waves with Metasurfaces," *Adv. Opt. Mater.*, vol. 4, pp. 818-833, 2016.
- [97] H.-T. Chen, A. J. Taylor and N. Yu, "A review of metasurfaces: physics and applications," *Rep. Prog. Phys.*, vol. 79, p. 076401, 2016.
- [98] S. B. Glybovski, S. A. Tretyakov, P. A. Belov, et al., "Metasurfaces: From microwaves to visible," *Phys. Rep.*, vol. 634, pp. 1-72, 2016.
- [99] S. M. Kamali, E. Arbabi, A. Arbabi, et al., "A review of dielectric optical metasurfaces for wavefront control," *Nanophotonics*, vol. 7, pp. 1041-1068, 2018.
- [100] N. Yu and F. Capasso, "Flat optics with designer metasurfaces," *Nat. Mater.*, vol. 13, pp. 139-150, 2014.
- [101] P. Genevet and F. Capasso, "Holographic optical metasurfaces: a review of current progress," *Rep. Prog. Phys.*, vol. 78, p. 024401, 2015.
- [102] D. Attwood and A. Sakdinawat, *X-rays and extreme ultraviolet radiation: principles and applications*. Cambridge University Press: 2017.
- [103] C. Zhang, S. Divitt, Q. Fan, et al., "Low-loss metasurface optics down to the deep ultraviolet region," *Light: Sci. Appl.*, vol. 9, pp. 1-10, 2020.
- [104] Y. Deng, X. Wang, Z. Gong, et al., "All-Silicon Broadband Ultraviolet Metasurfaces," *Adv. Mater.*, vol. 30, p. 1802632, 2018.
- [105] Y. Mao, D. Zhao, S. Yan, et al., "A vacuum ultraviolet laser with a submicrometer spot for spatially resolved photoemission spectroscopy," *Light: Sci. Appl.*, vol. 10, p. 22, 2021.
- [106] K. Huang, J. Deng, H. S. Leong, et al., "Ultraviolet Metasurfaces of $\approx 80\%$ Efficiency with Antiferromagnetic Resonances for Optical Vectorial Anti-Counterfeiting," *Laser & Photonics Reviews*, vol. 13, p. 1800289, 2019.
- [107] O. Hemmatyar, S. Abdollahramezani, Y. Kiarashinejad, et al., "Full color generation with fano-type resonant HfO₂ nanopillars designed by a deep-learning approach," *Nanoscale*, vol. 11, pp. 21266-21274, 2019.
- [108] M. Khorasaninejad and K. B. Crozier, "Silicon nanofin grating as a miniature chirality-distinguishing beam-splitter," *Nat. Commun.*, vol. 5, p. 5386, 2014.
- [109] W. T. Chen, A. Y. Zhu, V. Sanjeev, et al., "A broadband achromatic metalens for focusing and imaging in the visible," *Nat. Nanotechnol.*, vol. 13, pp. 220-226, 2018.

- [110] S. Wang, P. C. Wu, V.-C. Su, et al., "A broadband achromatic metalens in the visible," *Nat. Nanotechnol.*, vol. 13, pp. 227-232, 2018.
- [111] P. Lalanne and P. Chavel, "Metalenses at visible wavelengths: past, present, perspectives," *Laser Photonics Rev.*, vol. 11, p. 1600295, 2017.
- [112] K. Huang, F. Qin, Hong Liu, et al., "Planar Diffractive Lenses: Fundamentals, Functionalities, and Applications," *Adv. Mater.*, vol. 30, p. 1704556, 2018.
- [113] L. Huang, X. Chen, H. Mühlenbernd, et al., "Dispersionless phase discontinuities for controlling light propagation," *Nano Lett.*, vol. 12, pp. 5750-5755, 2012.
- [114] M. Mehmood, S. Mei, S. Hussain, et al., "Visible - Frequency Metasurface for Structuring and Spatially Multiplexing Optical Vortices," *Adv. Mater.*, vol. 28, pp. 2533-2539, 2016.
- [115] A. Niv, G. Biener, V. Kleiner, et al., "Manipulation of the Pancharatnam phase in vectorial vortices," *Opt. Express*, vol. 14, pp. 4208-4220, 2006.
- [116] W. Luo, S. Sun, H.-X. Xu, et al., "Transmissive Ultrathin Pancharatnam-Berry Metasurfaces with nearly 100% Efficiency," *Phys. Rev. Appl.*, vol. 7, p. 044033, 2017.
- [117] Y. F. Yu, A. Y. Zhu, R. Paniagua - Domínguez, et al., "High - transmission dielectric metasurface with 2π phase control at visible wavelengths," *Laser Photonics Rev.*, vol. 9, pp. 412-418, 2015.
- [118] J. Li, G. Si, H. Liu, et al., "Resonance-free ultraviolet metaoptics via photon nanosieves," *Opt. Lett.*, vol. 44, pp. 3418-3421, 2019.
- [119] L. Drescher, O. Kornilov, T. Witting, et al., "Extreme-ultraviolet refractive optics," *Nature*, vol. 564, pp. 91-94, 2018.
- [120] M. Semmlinger, M. L. Tseng, J. Yang, et al., "Vacuum ultraviolet light-generating metasurface," *Nano Lett.*, vol. 18, pp. 5738-5743, 2018.
- [121] S. Sun, K.-Y. Yang, C.-M. Wang, et al., "High-efficiency broadband anomalous reflection by gradient meta-surfaces," *Nano Lett.*, vol. 12, pp. 6223-6229, 2012.
- [122] Y. Ra'di, D. L. Sounas and A. Alu, "Metagratings: Beyond the limits of graded metasurfaces for wave front control," *Phys. Rev. Lett.*, vol. 119, p. 067404, 2017.
- [123] A. Yulaev, W. Zhu, C. Zhang, et al., "Metasurface-Integrated Photonic Platform for Versatile Free-Space Beam Projection with Polarization Control," *ACS Photonics*, vol. 6, pp. 2902-2909, 2019.
- [124] N. Mahmood, M. Q. Mehmood and F. A. Tahir, "Diamond step-index nanowaveguide to structure light efficiently in near and deep ultraviolet regimes," *Sci. Rep.*, vol. 10, pp. 1-10, 2020.
- [125] D. Li, K. Jiang, X. Sun, et al., "AlGaIn photonics: recent advances in materials and ultraviolet devices," *Advances in Optics and Photonics*, vol. 10, pp. 43-110, 2018.
- [126] C. Xie, X.-T. Lu, X.-W. Tong, et al., "Recent Progress in Solar-Blind Deep-Ultraviolet Photodetectors Based on Inorganic Ultrawide Bandgap Semiconductors," *Adv. Funct. Mater.*, vol. 29, p. 1806006, 2019.
- [127] D.-B. Li, X.-J. Sun, Y.-P. Jia, et al., "Direct observation of localized surface plasmon field enhancement by Kelvin probe force microscopy," *Light: Sci. Appl.*, vol. 6, pp. e17038-e17038, 2017.
- [128] G. Bao, D. Li, X. Sun, et al., "Enhanced spectral response of an AlGaIn-based solar-blind ultraviolet photodetector with Al nanoparticles," *Opt. Express*, vol. 22, pp. 24286-24293, 2014.
- [129] Y. Wu, X.-J. Sun, Y.-P. Jia, et al., "Review of improved spectral response of ultraviolet photodetectors by surface plasmon," *Chin. Phys. B*, vol. 27, p. 126101, 2018.
- [130] K. Kneipp, M. Moskovits and H. Kneipp, *Surface-enhanced Raman scattering: physics and applications*. Springer: 2006; Vol. 103.
- [131] R. Wen and Y. Fang, "Surface Raman scattering studies on the adsorption of p-hydroxybenzoic acid at Au electrodes with ultraviolet excitation," *J. Electroanal. Chem.*, vol. 576, pp. 237-242, 2005.
- [132] T. Dörfer, M. Schmitt and J. Popp, "Deep-UV surface-enhanced Raman scattering," *J. Raman Spectrosc.*, vol. 38, pp. 1379-1382, 2007.

- [133] A. Taguchi, N. Hayazawa, K. Furusawa, et al., "Deep-UV tip-enhanced Raman scattering," *J. Raman Spectrosc.*, vol. 40, pp. 1324-1330, 2009.
- [134] S. K. Jha, Z. Ahmed, M. Agio, et al., "Deep-UV Surface-Enhanced Resonance Raman Scattering of Adenine on Aluminum Nanoparticle Arrays," *J. Am. Chem. Soc.*, vol. 134, pp. 1966-1969, 2012.
- [135] A. Arbabi, E. Arbabi, S. M. Kamali, et al., "Miniature optical planar camera based on a wide-angle metasurface doublet corrected for monochromatic aberrations," *Nat. Commun.*, vol. 7, p. 13682, 2016.
- [136] S. Colburn, A. Zhan and A. Majumdar, "Metasurface optics for full-color computational imaging," *Sci. Adv.*, vol. 4, p. eaar2114, 2018.
- [137] H. Liang, Q. Lin, X. Xie, et al., "Ultrahigh Numerical Aperture Metalens at Visible Wavelengths," *Nano Lett.*, vol. 18, pp. 4460-4466, 2018.
- [138] K. Huang, H. F. Gao, G. W. Cao, et al., "Design of DPE for modulating the electric field at the out-of-focus plane in a lens system," *Appl. Opt.*, vol. 51, pp. 5149-5153, 2012.
- [139] L. Huang, X. Chen, H. Mühlenbernd, et al., "Three-dimensional optical holography using a plasmonic metasurface," *Nat. Commun.*, vol. 4, p. 2808, 2013.
- [140] D. Wen, F. Yue, G. Li, et al., "Helicity multiplexed broadband metasurface holograms," *Nat Commun*, vol. 6, p. 8241, 2015.
- [141] K. Huang, Chirality and Antiferromagnetism in Optical Metasurfaces. In *Chirality, Magnetism and Magnetolectricity*, Kamenetskii, E., Ed. Springer Nature Switzerland AG: 2021.
- [142] A. Nemati, Q. Wang, M. Hong, et al., "Tunable and reconfigurable metasurfaces and metadevices," *Opto-Electronic Advances*, vol. 1, p. 180009, 2018.
- [143] X. Zhou, S. He, G. Liu, et al., "New developments in laser-based photoemission spectroscopy and its scientific applications: a key issues review," *Rep. Prog. Phys.*, vol. 81, p. 062101, 2018.
- [144] G. Liu, G. Wang, Y. Zhu, et al., "Development of a vacuum ultraviolet laser-based angle-resolved photoemission system with a superhigh energy resolution better than 1meV," *Rev. Sci. Instrum.*, vol. 79, p. 023105, 2008.
- [145] H. Iwasawa, E. F. Schwier, M. Arita, et al., "Development of laser-based scanning μ -ARPES system with ultimate energy and momentum resolutions," *Ultramicroscopy*, vol. 182, pp. 85-91, 2017.
- [146] I. Cucchi, I. Gutiérrez-Lezama, E. Cappelli, et al., "Microfocus laser-angle-resolved photoemission on encapsulated mono-, bi-, and few-layer $1T'$ -WTe₂," *Nano Lett.*, vol. 19, pp. 554-560, 2018.
- [147] F. Qin, K. Huang, J. Wu, et al., "Shaping a Subwavelength Needle with Ultra-long Focal Length by Focusing Azimuthally Polarized Light," *Sci. Rep.*, vol. 5, p. 09977, 2015.
- [148] Z. Wang, G. Yuan, M. Yang, et al., "Exciton-Enabled Meta-Optics in Two-Dimensional Transition Metal Dichalcogenides," *Nano Lett.*, vol. 20, pp. 7964-7972, 2020.
- [149] G. H. Yuan, E. T. Rogers and N. I. Zheludev, "Achromatic super-oscillatory lenses with sub-wavelength focusing," *Light: Sci. Appl.*, vol. 6, p. e17036, 2017.
- [150] H. Liu, M. Q. Mehmood, K. Huang, et al., "Twisted focusing of optical vortices with broadband flat spiral zone plates," *Adv. Opt. Mater.*, vol. 2, pp. 1193-1198, 2014.
- [151] K. Huang, H. Liu, G. Si, et al., "Photon-nanosieve for ultrabroadband and large-angle-of-view holograms," *Laser Photonics Rev.*, vol. 11, p. 1700025, 2017.
- [152] K. Huang, H. Liu, F. J. Garcia-Vidal, et al., "Ultrahigh-capacity non-periodic photon sieves operating in visible light," *Nat. Commun.*, vol. 6, p. 7059, 2015.
- [153] S. Mei, M. Q. Mehmood, S. Hussain, et al., "Flat Helical Nanosieves," *Adv. Fun. Mater.*, vol. 26, pp. 5255-5262, 2016.
- [154] Y. J. Liu, H. Liu, E. S. P. Leong, et al., "Fractal Holey Metal Microlenses with Significantly Suppressed Side Lobes and High - Order Diffractions in Focusing," *Adv. Opt. Mater.*, vol. 2, pp. 487-492, 2014.
- [155] L. Kipp, M. Skibowski, R. L. Johnson, et al., "Sharper images by focusing soft X-rays with photon sieves," *Nature*, vol. 414, pp. 184-188, 2001.

- [156] C. W. Hsu, B. Zhen, A. D. Stone, et al., "Bound states in the continuum," *Nat. Rev. Mater.*, vol. 1, p. 16048, 2016.
- [157] C. Huang, C. Zhang, S. Xiao, et al., "Ultrafast control of vortex microlasers," *Science*, vol. 367, pp. 1018-1021, 2020.
- [158] J. Hu, M. Lawrence and J. A. Dionne, "High Quality Factor Dielectric Metasurfaces for Ultraviolet Circular Dichroism Spectroscopy," *ACS Photonics*, vol. 7, pp. 36-42, 2020.
- [159] V. R. Manfrinato, J. Wen, L. Zhang, et al., "Determining the Resolution Limits of Electron-Beam Lithography: Direct Measurement of the Point-Spread Function," *Nano Lett.*, vol. 14, pp. 4406-4412, 2014.
- [160] Y. Deng, Q. Huang, Y. Zhao, et al., "Precise fabrication of a 5 nm graphene nanopore with a helium ion microscope for biomolecule detection," *Nanotechnology*, vol. 28, p. 045302, 2016.
- [161] T. H. Erika, D. J. April, A. S. Charles, et al., "Charge-coupled devices detectors with high quantum efficiency at UV wavelengths," *J. Astron. Telesc. Instrum. Syst.*, vol. 2, pp. 1-11, 2016.
- [162] T. Masuzawa, M. Onishi, I. Saito, et al., "High quantum efficiency UV detection using a-Se based photodetector," *physica status solidi (RRL) – Rapid Research Letters*, vol. 7, pp. 473-476, 2013.
- [163] T. Masuzawa, S. Kuniyoshi, M. Onishi, et al., "Conditions for a carrier multiplication in amorphous-selenium based photodetector," *Appl. Phys. Lett.*, vol. 102, p. 073506, 2013.
- [164] X. Yang and D. Wang, "Photocatalysis: From Fundamental Principles to Materials and Applications," *ACS Applied Energy Materials*, vol. 1, pp. 6657-6693, 2018.
- [165] C. Wang, W.-C. D. Yang, D. Raciti, et al., "Endothermic reaction at room temperature enabled by deep-ultraviolet plasmons," *Nat. Mater.*, vol., pp. 1-7, 2020.
- [166] S.-L. Yu and S.-K. Lee, "Ultraviolet radiation: DNA damage, repair, and human disorders," *Mol. Cell. Toxicol.*, vol. 13, pp. 21-28, 2017.
- [167] J. Bai, X. Zhong, S. Jiang, et al., "Graphene nanomesh," *Nat. Nanotechnol.*, vol. 5, pp. 190-194, 2010.
- [168] M. Corso, W. Auwärter, M. Muntwiler, et al., "Boron nitride nanomesh," *Science*, vol. 303, pp. 217-220, 2004.
- [169] C. W. Hsu, B. Zhen, A. D. Stone, et al., "Bound states in the continuum," *Nat. Rev. Mater.*, vol. 1, pp. 1-13, 2016.
- [170] Y. Yang, J. Lu, A. Manjavacas, et al., "High-harmonic generation from an epsilon-near-zero material," *Nat. Phys.*, vol. 15, pp. 1022-1026, 2019.
- [171] P. Wang, Y. Zheng, X. Chen, et al., "Localization and delocalization of light in photonic moiré lattices," *Nature*, vol. 577, pp. 42-46, 2020.
- [172] Z. Xu and B. M. Sadler, "Ultraviolet Communications: Potential and State-Of-The-Art," *IEEE Communications Magazine*, vol. 46, pp. 67-73, 2008.
- [173] K. Deisseroth, "Optogenetics," *Nat. Methods*, vol. 8, pp. 26-29, 2011.
- [174] K. Zoschke, N. Dietrich, H. Börnick, et al., "UV-based advanced oxidation processes for the treatment of odour compounds: Efficiency and by-product formation," *Water Res.*, vol. 46, pp. 5365-5373, 2012.
- [175] S. A. Asher, "UV resonance Raman spectroscopy for analytical, physical, and biophysical chemistry. Part 1," *Anal. Chem.*, vol. 65, pp. 59A-66A, 1993.
- [176] M. J. Dodge, "Refractive properties of magnesium fluoride," *Appl. Opt.*, vol. 23, pp. 1980-1985, 1984.
- [177] L. Guo, S. Xu, R. Wan, et al., "Design of aluminum nitride metalens in the ultraviolet spectrum," *Journal of Nanophotonics*, vol. 12, p. 043513, 2018.
- [178] F. Matusalem, M. Marques, L. K. Teles, et al., "Electronic properties of fluorides by efficient approximated quasiparticle DFT-1/2 and PSIC methods: BaF₂, CaF₂ and CdF₂ as test cases," *J. Phys.: Condens. Matter*, vol. 30, p. 365501, 2018.

Figures and Captions

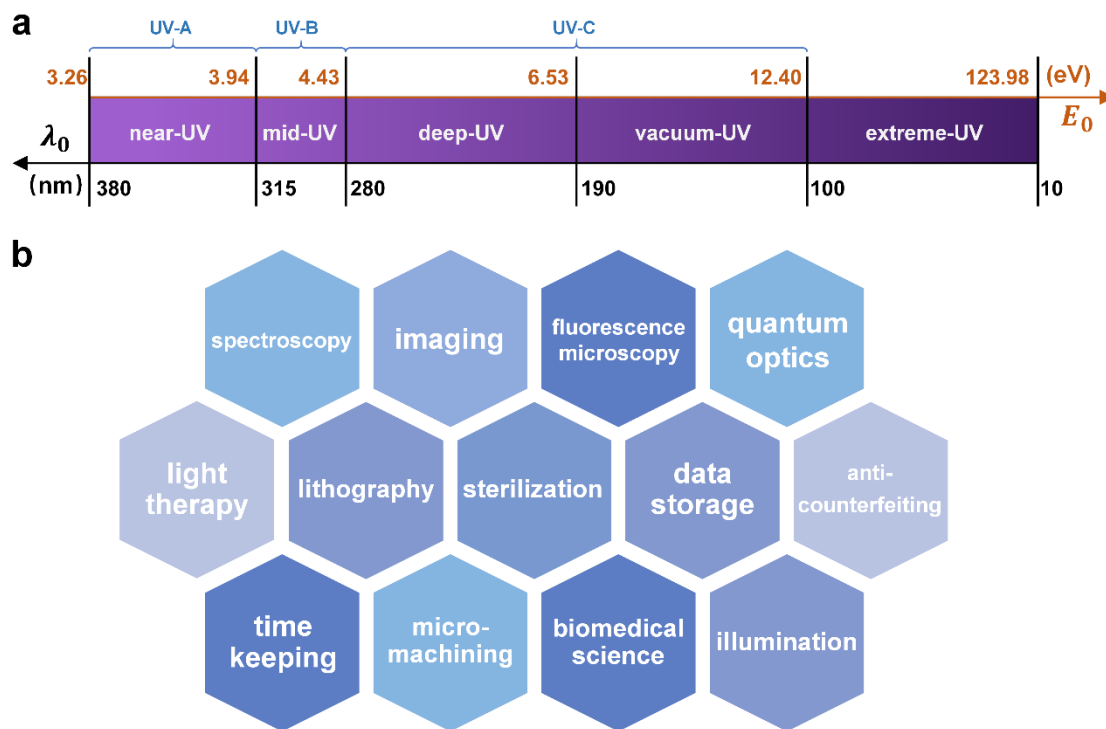


Fig. 1. (a) Electromagnetic spectrum for the UV range and the constituent five sub-bands. **(b)** Representative applications of UV radiation.

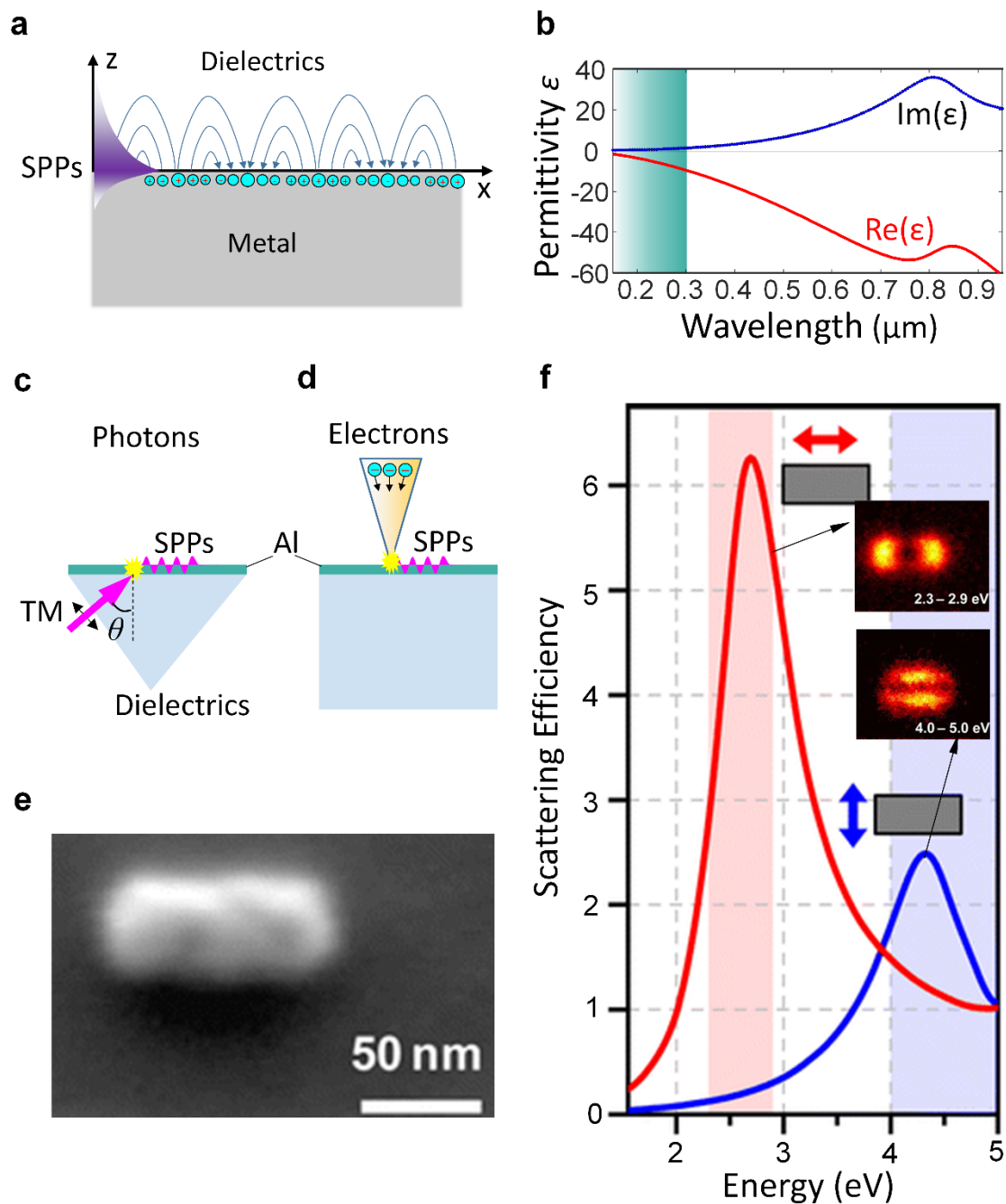


Fig. 2. (a) Sketch for SPPs at the interface between dielectric and metal. (b) Permittivity of aluminum. (c-d) Sketch for the excitons of UV SPPs by using photons (c) and electrons (d). (e) SEM images of an Aluminum nanoparticle. (f) The simulated scattering intensity for the longitudinal (red) and transverse (blue) plasmonic modes existing in the nanoparticle in (e). Knight et al. [41]. © 2012 American Chemical Society. The inserts show the experimental measured plasmonics modes by using different filters.

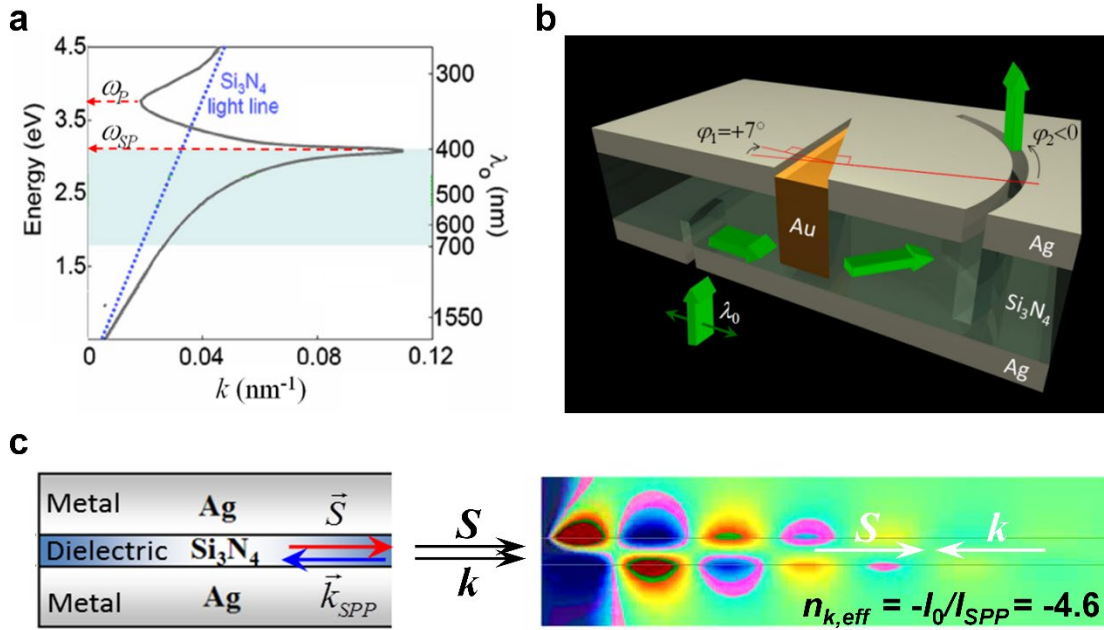


Fig. 3. (a) Dispersion diagram for a plasmon mode in an MDM waveguide composed of Ag-Si₃N₄-Ag. **Lezec et al.[48]. © 2007 The American Association for the Advancement of Science. (b)** Schematic drawing of negative refraction using Au-prism in an MDM waveguide. **(c)** Finite-difference-time-domain (FDTD)-calculated magnetic field distribution of the plasmon mode in an MDM waveguide when excited at normal incidence from free-space at $\lambda_0 = 514$ nm.

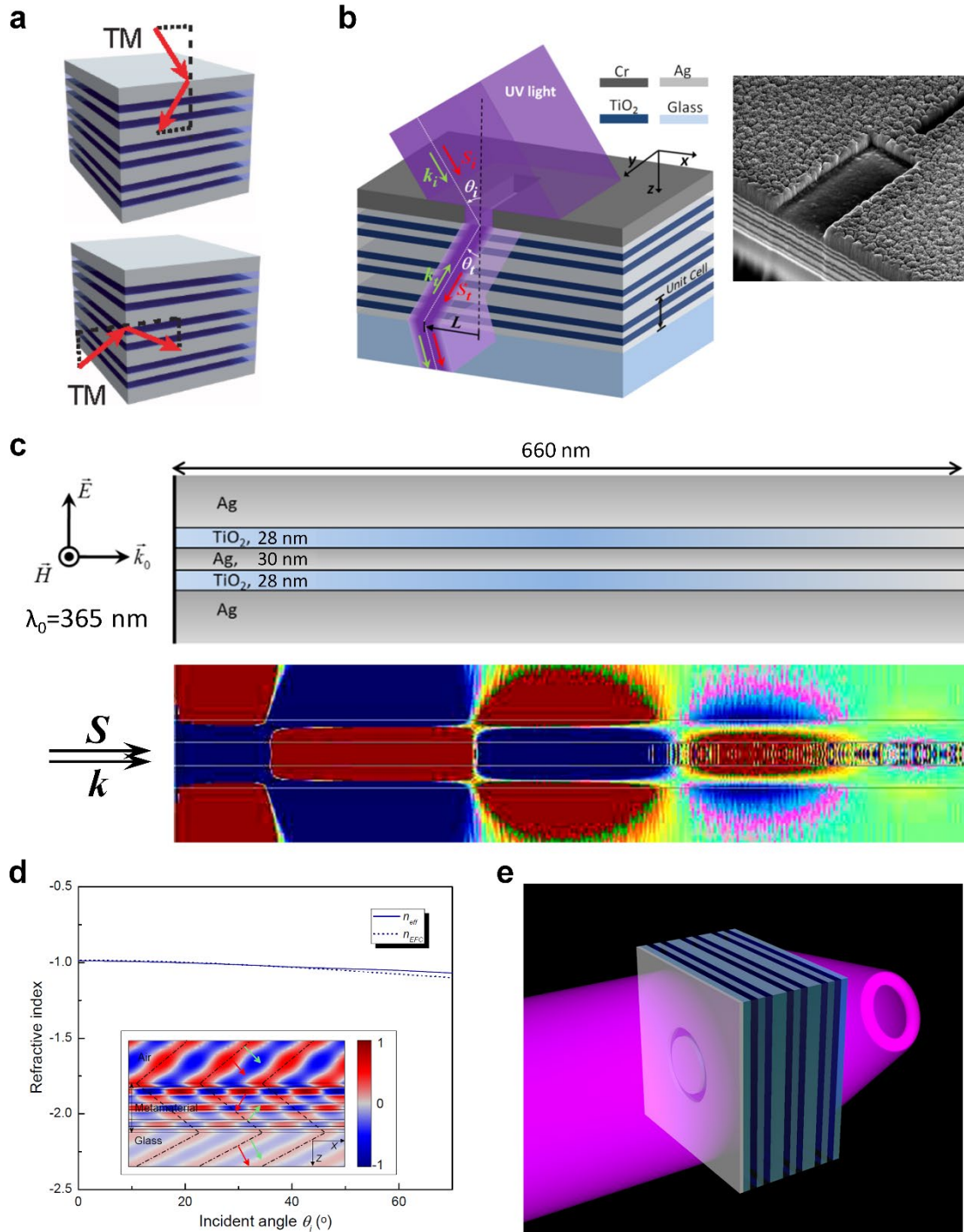


Fig. 4. (a) Schematic drawing of all-angle negative refraction for a stack of three MDMDM unit-cells for excitation along the plane of the layers (upper panel), and orthogonal to them (lower panel). TM polarized light is utilized in both cases. Verhagen et al. [49]. © 2010 American Physical Society. **(b)** Left: schematic drawing of negative refraction from air into a metamaterial formed by three vertically stacked unit cells, each consisting of planar layers of Ag-TiO₂-Ag-TiO₂-Ag. The

structure is coated with a beam-defining mask consisting of a rectangular aperture (width: 600 nm, length: 10 μm) in an opaque Cr film (thickness: 120 nm). Right: scanning electron microscopy image of cross-section of a fabricated device. **(c)** FDTD-calculated magnetic field distribution of the plasmon mode in an MDMDM waveguide when excited at normal incidence from free-space at $\lambda_0 = 364$ nm. **(d)** Experimental values of refractive index (solid curve), and numerical values of refractive index (dotted curve), as a function of angle of incidence θ_i , for TM-polarized light. Inset: FDTD-simulated magnetic field distribution for $\theta_i = 40^\circ$. **Xu et al. [50]. © 2013 Springer Nature.** **(e)** Schematic drawing of a flat lens illuminated with UV light (purple). A sample object of ring shape placed on one side of the flat lens is projected as a three-dimensional image in free space on the other side of the lens.

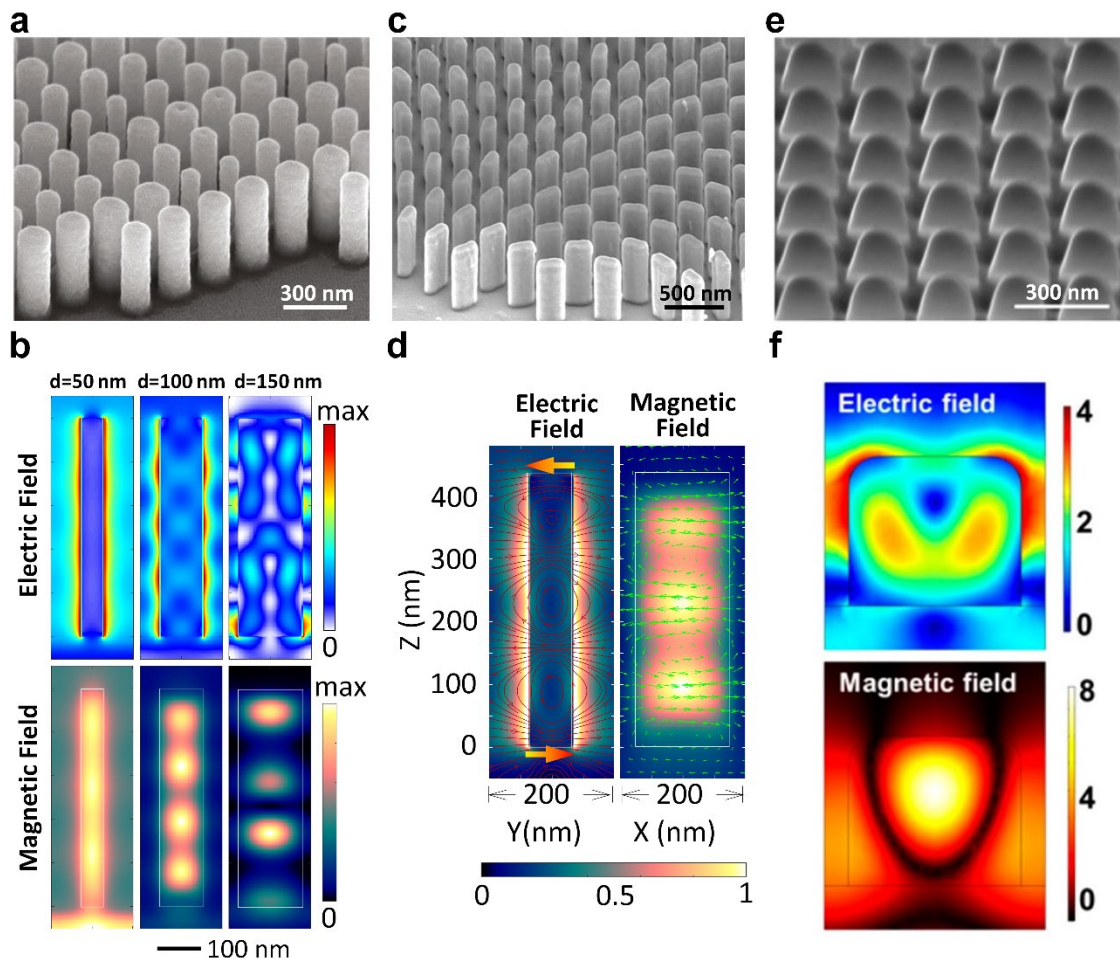


Fig. 5. (a-b) SEM image (a) of HfO_2 -based waveguide metasurfaces and the electromagnetic nanomodes (b) resonating in the nanopyllars with different diameters ranging from $d=50$ nm to 150

nm. **Zhang et al. [103]. Author copyright.** (c-d) SEM image (c) of Nb₂O₅-based geometric metasurfaces and the antiferromagnetic resonances (d) in the nanostructures under the illumination of γ -polarized light. **Huang et al. [106]. © 2019, WILEY-VCH Verlag GmbH & Co. KGaA, Weinheim.** (e-f) SEM image (e) of the ZnO-based resonance metasurfaces and the simulated magnetic dipoles (f) confined in the nanostructure. **Semmlinger et al. [120]. © 2018 American Chemical Society.**

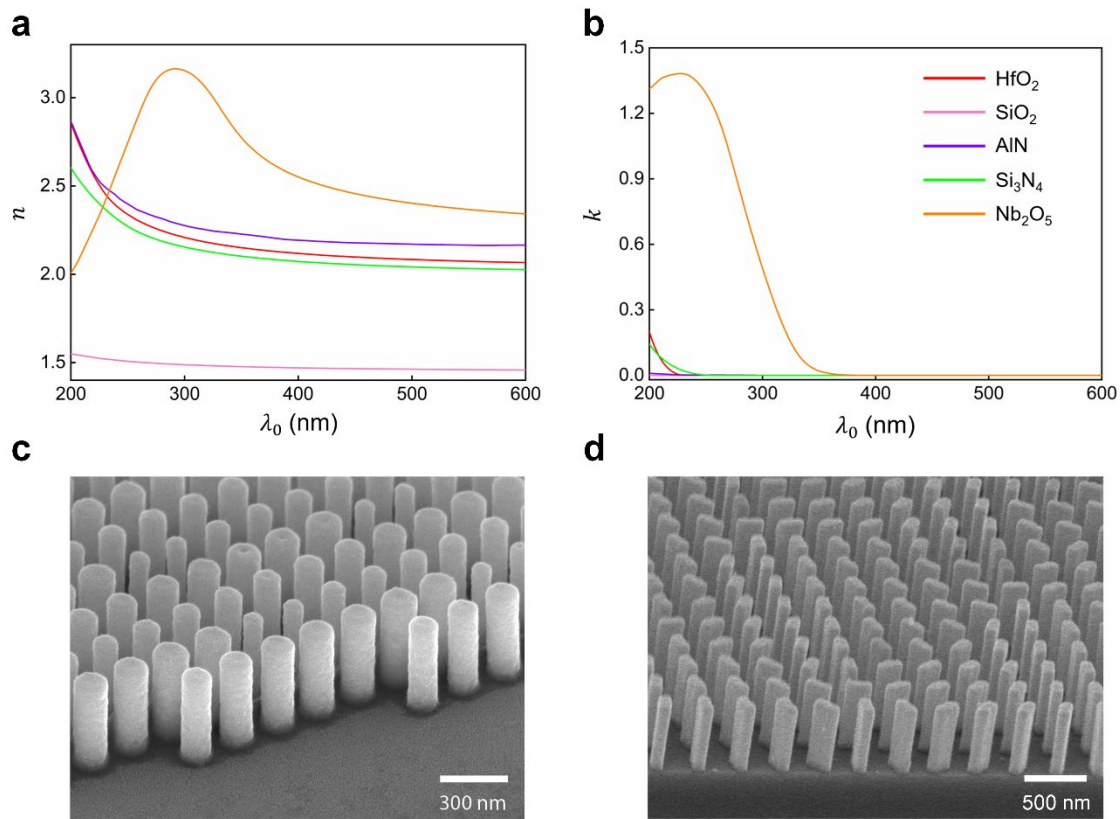


Fig. 6. (a-b) Refractive index n (a) and extinction coefficient k (b) of representative UV-transparent dielectric materials. The legend in Fig. 6b applies to Fig. 6a. **(c)** Scanning electron microscopy image of a HfO₂-based metasurface operating in the deep-UV. **Zhang et al. [103]. Author copyright.** **(d)** Scanning electron microscopy image of a Nb₂O₅-based metasurface operating in the near-UV. **Huang et al. [106]. © 2019, WILEY-VCH Verlag GmbH & Co. KGaA, Weinheim.**[38, 48, 77, 103, 106, 124, 176-178]

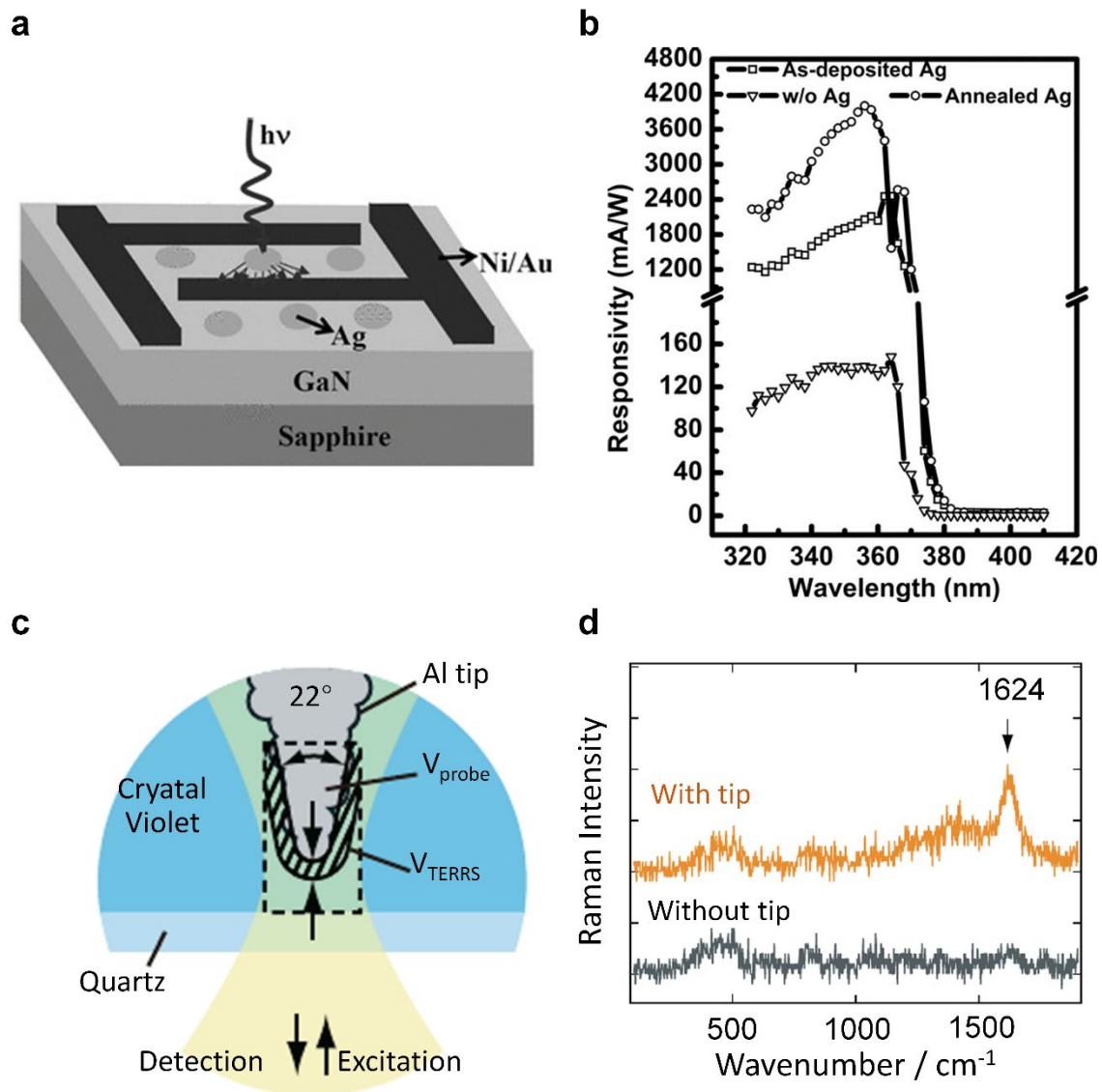


Fig. 7. (a-b) A GaN-based UV photodetector with plasmonic enhancement via Ag nanoparticles **(a)** and its measured responsivity at the UV wavelengths **(b)**. Li et al.[38]. © 2012 WILEY-VCH Verlag GmbH & Co. KGaA, Weinheim. **(c-d)** Tip-enhanced Raman scattering spectroscopy **(c)** and a comparison of the experimental Raman intensity between the cases with and without tip **(d)**. © 2009 John Wiley & Sons, Ltd.

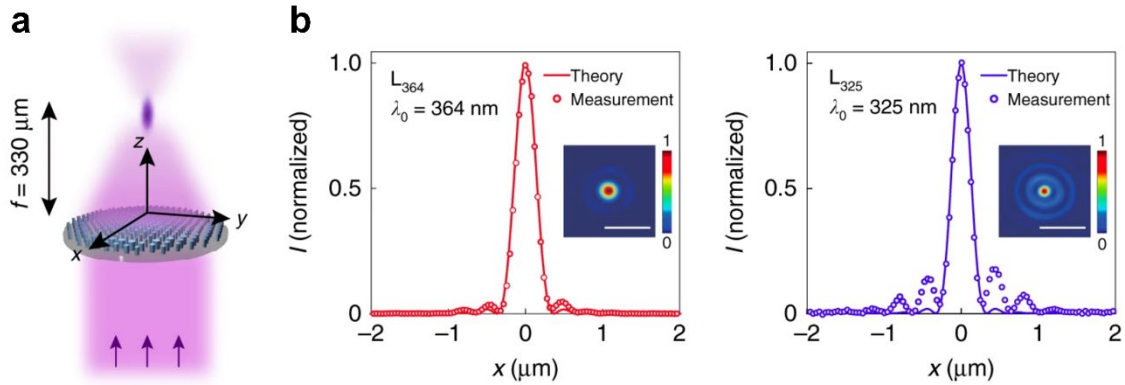


Fig. 8. (a) Schematic drawing of focusing by a UV metalens, L_{364} or L_{325} , under normal-incidence, plane-wave illumination at free-space wavelength of $\lambda_0 = 364 \text{ nm}$ or 325 nm , respectively. (b-c) Cross-focus cuts and intensity distributions in the focal plane, as measured for metalenses L_{364} and L_{325} , respectively. The theoretically predicted cross-focus cuts are plotted for reference. Scale bars: $1 \mu\text{m}$. Zhang et al. [103]. Author copyright.

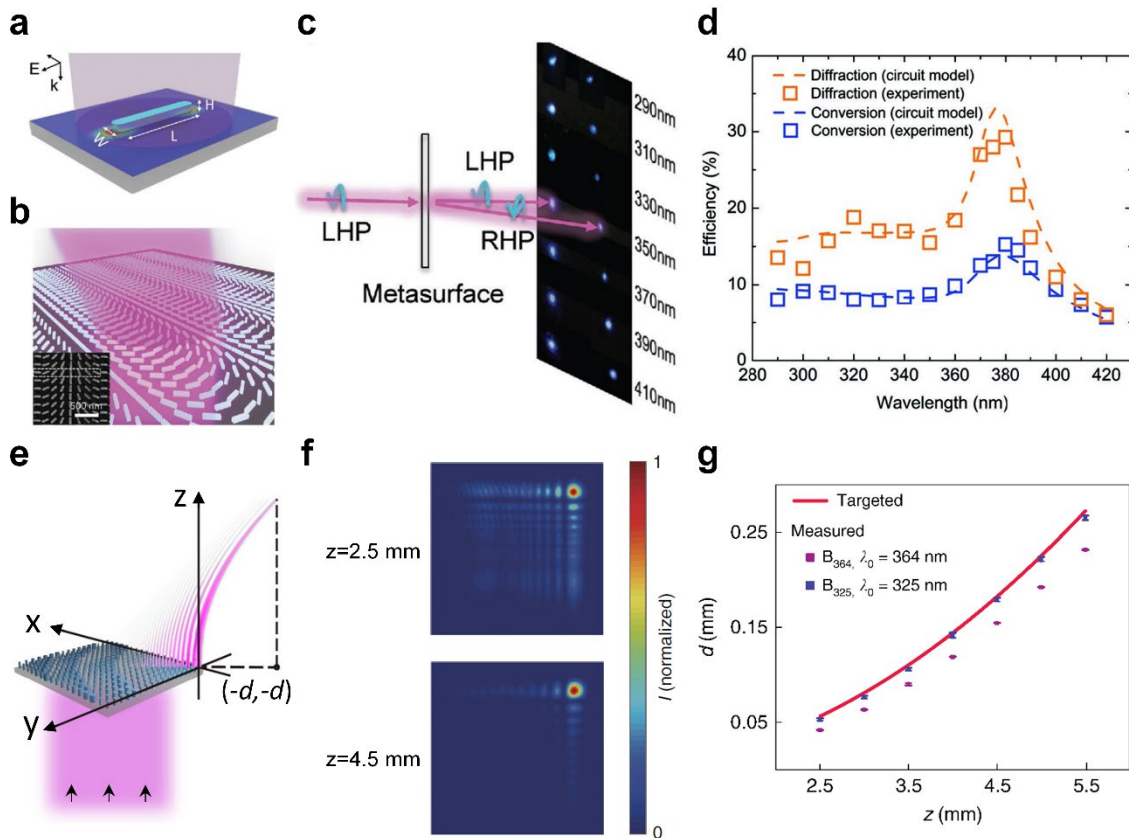


Fig. 9. Beam steering by using ultraviolet metasurfaces. (a) Sketch for the working principle of Si-based ultraviolet geometric metasurfaces. (b) Image of ultraviolet metasurfaces for beam steering.

(c) Experimental results for steering the ultraviolet at the different wavelengths. (d) Measured efficiency of this metasurfaces over a broadband spectrum. **Deng et al. [104]. © 2018 WILEY-VCH Verlag GmbH & Co. KGaA, Weinheim.** (e-f) Sketch for steering the beam along a curved trajectory (e) via the Airy beam (f). (g) A comparison between the experimental and ideal trajectories at the different z cut planes. **Zhang et al. [103]. Author copyright.**

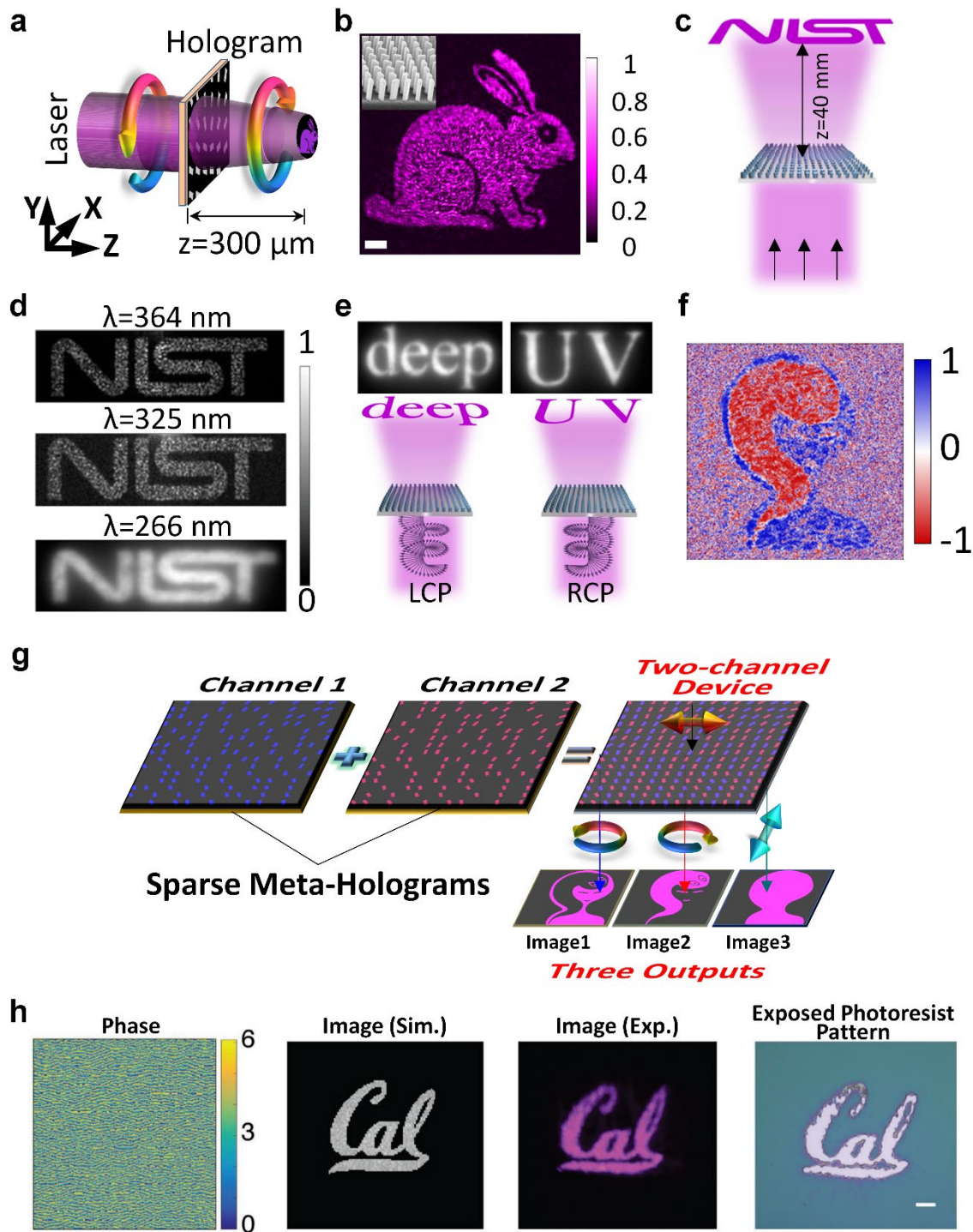


Fig. 10. (a-b) Sketch (a) for the ultraviolet metasurface hologram and the experimental holographic image (b) by using the Nb_2O_5 nanobricks at the operating wavelength of 355 nm. **Huang et al. [106].** © 2019, WILEY-VCH Verlag GmbH & Co. KGaA, Weinheim. (c-d) Sketch (c) for the HfO_2 -based meta-hologram operating at the broadband wavelengths and their measured images (d). (e)

Spin-multiplexed metahologram that reconstructs two spin-dependent images at the wavelength of 266 nm. **Zhang et al. [103]. Author copyright.** (f) Spin-multiplexed ultraviolet metasurfaces encoding two sparse holograms that are used to create the complementary images of “girl” and “snake”. (g) Experimental holographic image by labelling the polarization information where the blue color denotes the spin-up photons and the red for spin-down photons. **Huang et al. [106]. © 2019, WILEY-VCH Verlag GmbH & Co. KGaA, Weinheim.** (h) Si-based ultraviolet metahologram for lithography. The phase profile of the hologram is shown at the left panel. The simulated, experimental and exposed images are provided at the right panel by addressing their names. **Deng et al. [104]. © 2018 WILEY-VCH Verlag GmbH & Co. KGaA, Weinheim.**

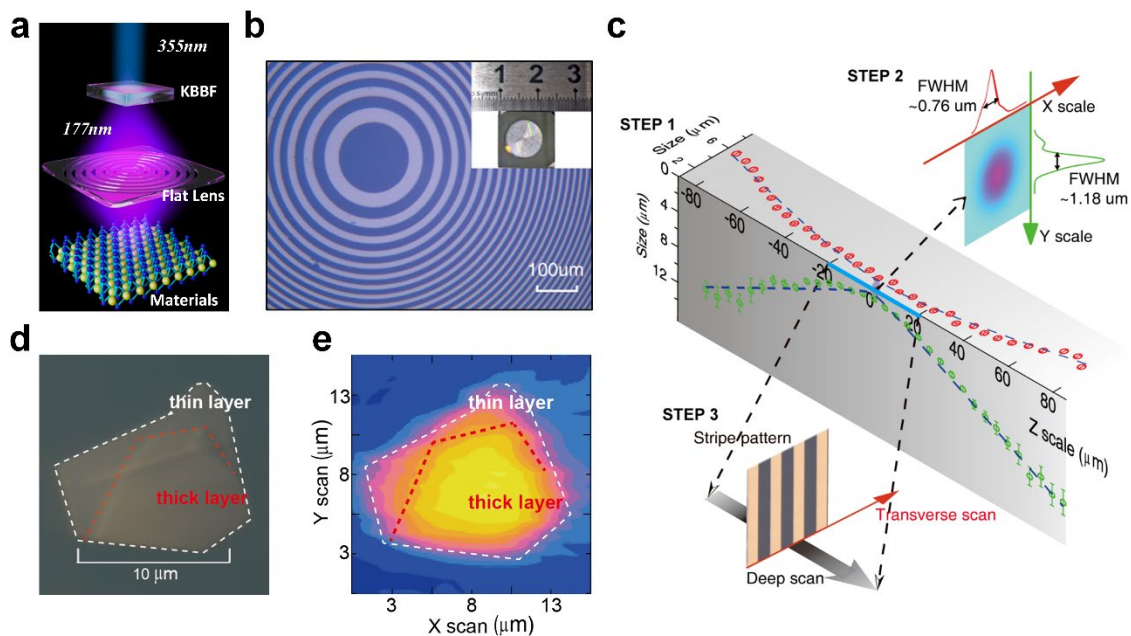


Fig. 11. Photoemission spectroscopy with a sub-micrometer spot created by focusing the vacuum ultraviolet laser with a zone-plate flat lens. (a) Sketch of the spectroscopy. (b) Microscopy image of fabricated lens. (c) The experimental measured focal spot around the focal plane. (d-e) The microscopy (d) and scanned (e) images of the graphene flakes. The transmission of the scanned image can be used to calculate the layer number of the graphene flakes. **Mao et al. [105]. Author copyright.**

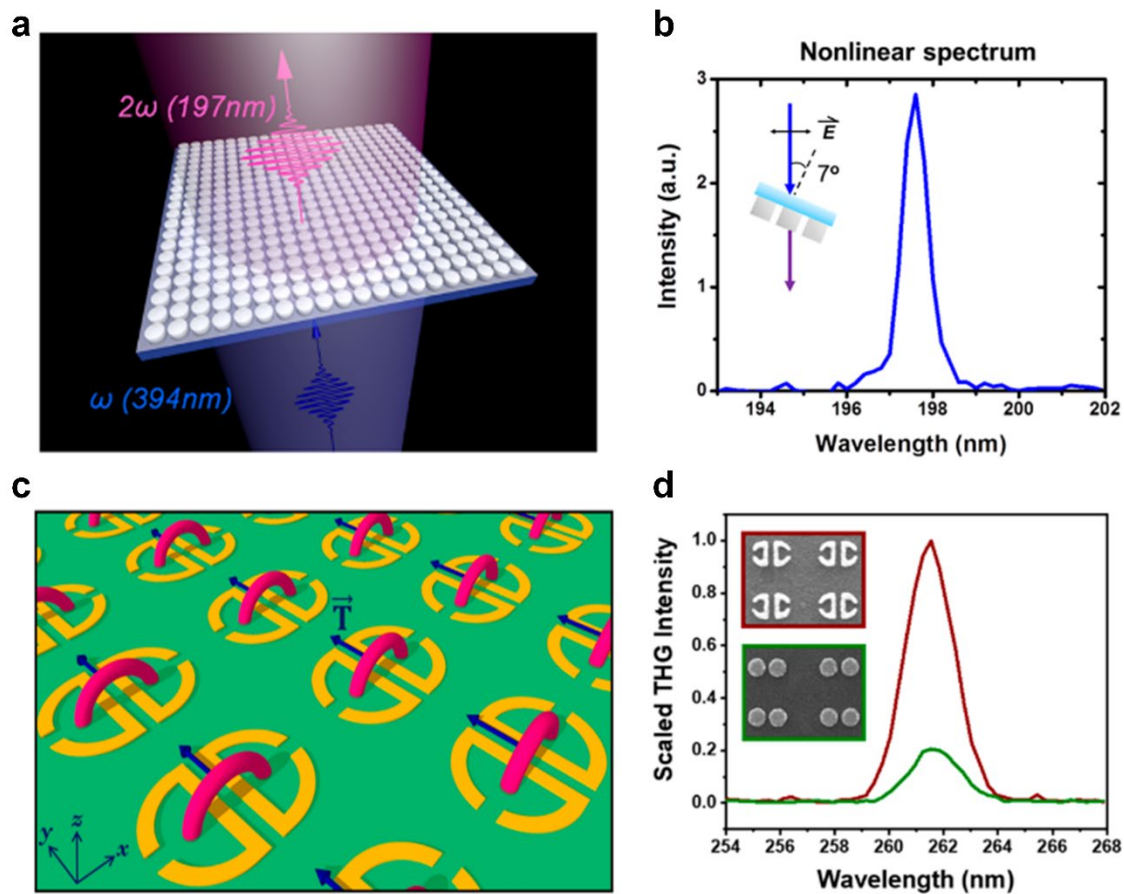


Fig. 12. Nonlinear ultraviolet metasurfaces. (a-b) Second harmonic generation (a) by using the ZnO-based metasurfaces and the yielded SHG intensity (b). **Semmlinger et al. [120]. © 2018 American Chemical Society.** (c) Third harmonic generation assisted by the toroidal dipole to enhance the THG signal (c). (d) A comparison between the THG signals created by the toroidal meta-atoms (red) and nanodisk (green) dimers. **Ahmadvand et al. [37]. © 2019, American Chemical Society.**